

Abundances of refractory ions in Beta Pictoris exocomets

T. Vrignaud¹, A. Lecavelier des Etangs¹, P. A. Strøm², and F. Kiefer³

¹ Institut d'Astrophysique de Paris, CNRS, UMR 7095, Sorbonne Université, 98^{bis} boulevard Arago, 75014 Paris, France

² Department of Physics, University of Warwick, Coventry CV4 7AL, UK

³ LESIA, Observatoire de Paris, Université PSL, CNRS, 5 Place Jules Janssen, 92190 Meudon, France

March 24, 2025

ABSTRACT

β Pictoris is a young, A5V star, known for harbouring a large number of cometary-like object (or exocomets) which frequently transit the star and create variable absorption signatures in its spectrum. The physical and chemical properties of these exocomets can be probed by the recently introduced curve of growth approach, which enables column densities measurements in cometary tails using absorption measurements in numerous spectral lines. Using this approach, we present a new study of archival spectra of β Pic obtained with the *Hubble* Space Telescope, the HARPS spectrograph, and at the Mont John University Observatory, aimed at constraining the abundance of refractory ions in β Pic exocomets. 29 individual objects are studied, all observed in Fe II lines (used as a reference ion) and at least one other species (Ni II, Ca II, Cr II...). We find that the refractory composition of β Pic exocomets is overall stable, especially for singly ionised species, and consistent with solar abundances. This validates the use of the curve of growth approach to study exocometary composition. We also show that some ions, such as Ca II, are significantly depleted compared to solar abundances, which allows us to constrain the typical ionisation state in β Pic exocomets. We find that most refractory elements (Mg, Ni, Fe...) are split in similar fractions between their first and second ionisation states, with the exception of Ca, mostly ionized twice. A strong correlation between the Al III/Fe II ratio and radial velocity is also found, showing that the most redshifted exocomets tend to be more ionised. These results open the way for further modelling of exocomets, in order to unveil their composition and the physical processes that affect their tails.

Key words. Techniques: spectroscopic - Stars: individual: β Pic - Comets: general - Exocomets - Transit spectroscopy

1. Introduction

β Pictoris (β Pic) is a well-studied young (20 Myr, Miret-Roig et al. 2020) planetary system, often considered a benchmark for studying planetary system formation and evolution. It has attracted significant attention due to its prominent debris disk (Smith & Terrile 1984), which is rich in gas and dust (Vidal-Madjar et al. 1986; Roberge et al. 2006; Apai et al. 2015) and extends over hundreds of au. The system is also known for hosting planets (Lagrange et al. 2010, 2019; Nowak et al. 2020) and a large number of exocomets (Ferlet et al. 1987; Zieba et al. 2019; Lecavelier des Etangs et al. 2022). In fact, β Pic is, by far, the star showing the most intense exocomet activity, with hundreds of objects detected so far using transit spectroscopy (Kiefer et al. 2014b). Other systems with reported exocomets (typically A-type stars, such as HD 172555 and 49 Cet) generally show much weaker activity (Kiefer et al. 2014a; Montgomery & Welsh 2012; Rebollido et al. 2020; Strøm et al. 2020). Exocomets are of high scientific interest, as they provide valuable insights into the physical and dynamical processes occurring in the early stages of planetary system evolution. For instance, it has been proposed that the presence of exocomets in the inner region of the β Pic system is linked to the gravitational perturbation of planets, which can elongate the orbits of small bodies formed at large stellar distances and bring them to the stellar vicinity (Beust & Morbidelli 1996; Beust et al. 2024). Hints of collisions in the β Pic system have also been reported (Rebollido et al. 2024; Chen et al. 2024), providing an alternative scenario for the origin of the exocomets. Yet, despite extensive observational campaigns over the past decades, the intrinsic properties

of the exocomets — such as their composition and production rates — have remained largely unknown. In particular, no abundance measurements have been conducted so far, depriving us of key information to understand their nature and origin.

A significant advancement in the study of exocomets came with the work of Vrignaud et al. (2024a), who introduced a new approach for analysing spectroscopic transit data, termed the "exocomets curve of growth". This approach is based on the fact that the absorption depth of a transiting comet in a set of lines from a fixed species (eg. Fe II) is generally a simple function of the lines parameters (oscillator strength, excitation energy). The comet's absorption depths can thus be easily fitted to extract the main physical properties of the comet (covering factor, column density) and to infer critical information about the excitation states of ions within the transiting gas.

By applying this approach to a comet observed on December 6, 1997, the most recent study of Vrignaud & Lecavelier des Etangs (2024) showed that the gas excitation in β Pic exocomets is primarily controlled by the photon flux received from the star, rather than by electronic collisions. In this so-called radiative regime, the excitation temperature of the gas is set to the stellar effective temperature (~ 8000 K); the excitation state is thus de-correlated from the local properties of the gas (density, kinetic temperature). This regime is typically associated with a low electronic density ($n_e \leq 10^7$ cm⁻³) and close transit distance ($d \leq 60R_*$). The study of Vrignaud & Lecavelier des Etangs (2024) also showed that the various ions (e.g. Fe II, Cr II, Ni II...) detected in the December 1997 comet are characterised by similar radial velocity profiles and excitation states, hinting that they are well-mixed. This shared behaviour among the ob-

served ions is of great use for estimating their abundance ratios in exocomets. For instance, the Ni^+/Fe^+ and Cr^+/Fe^+ ratios in the December 6, 1997 comet were estimated to be $8.5 \pm 0.8 \cdot 10^{-2}$ and $1.04 \pm 0.15 \cdot 10^{-2}$ respectively, rather close to the solar Ni/Fe and Cr/Fe values (Vrignaud & Lecavelier des Etangs 2024).

In this paper, we aim to apply the exocomet curve of growth method to all the exocomets detected so far with the Space Telescope Imaging Spectrograph (STIS) onboard the Hubble Space Telescope (HST). By analysing the absorption features observed in an extended list of lines from a dozen of chemical species, we aim to place strong constraints on the composition of the cometary tails that routinely transit β Pic. This comprehensive analysis will allow us to investigate the physical mechanisms that affect the composition of these tails (e.g. ionisation), and to further our understanding of the chemical diversity within the β Pic system.

The set of observations used in our analysis is presented in Sect. 2. Sections 3 and 4 then describe our modified curve of growth model, aimed at analysing several species in a given exocomet simultaneously, and its application to a selection of 29 β Pic exocomets observed with the HST. The discussion and conclusion are provided in Sect. 5 and 6.

2. Studied observations

2.1. Raw data

Our study is primarily based on high resolution spectroscopic observations of β Pic obtained with the STIS spectrograph onboard the HST. Obtained between 1997 and 2024, these spectra cover wavelength ranges between 1600 and 3000 Å, and include a large number of spectral lines from various ionised species (Fe II, Ni II, Si II, Cr II...). These lines, particularly from Fe II, have been shown to be a powerful probe of the physical properties of the transiting comets (Vrignaud et al. 2024a; Vrignaud & Lecavelier des Etangs 2024).

Our dataset is completed with spectroscopic observations of β Pic obtained with other instruments, very close in time to the STIS data (typically a few hours apart). These additional observations were collected using the Cosmic Origins Spectrograph (COS), also aboard the HST, as well as the High Accuracy Radial Velocity Planet Searcher (HARPS) on the European Southern Observatory 3.6m telescope in La Silla, Chile, and the échelle spectrograph on the McLellan 1-m Telescope at the Mount John University Observatory (MJUO) in New Zealand. The COS spectra cover the far-ultraviolet (FUV) range ($\sim 1100 - 1500$ Å), while the HARPS and MJUO spectra probe the visible domain. These complementary datasets provide access to spectral lines that were never observed with STIS, such as the 1250 Å S II triplet (COS) and the 3900 Å Ca II doublet (HARPS, MJUO).

The COS and STIS data were retrieved from the MAST archive, while the HARPS data was obtained from the ESO science portal. The MJUO spectra were obtained from Tobin et al. (2019); only one night (December 6, 1997) was used in our study. A summary of the studied observations is provided in Table B.1.

2.2. Data Reduction

The HARPS and STIS data were reduced in a similar manner as that described in Vrignaud et al. (2024a). First, the different spectral orders of each spectrum were weighted together and re-sampled on a common wavelength table. Then, to correct from flux calibration disparity from one observation to another, each

spectrum was renormalised by a cubic spline fitted to stable spectral regions (see Fig. 1 of Vrignaud et al. 2024a). Finally, each set of spectra collected during a short time frame (e.g. the December 6 and December 19, 1997 HST visits) was averaged together, to boost their Signal-to-Noise ratio (S/N) and facilitate their analysis. The COS spectra were simply renormalised by their mean value in the 1350-1380 Å range, which does not show spectral variations due to exocomets. Contrary to STIS and HARPS, no chromatic variation of flux calibration was found for the COS data. The MJUO spectra were not renormalized, as Tobin et al. (2019) already provide flux-calibrated data. Finally, all spectra were shifted to the rest frame of β Pic, assuming an heliocentric radial velocity of 20 km/s (Gontcharov 2007).

2.3. Exocomet-free spectrum

Once the studied spectra have been renormalised to a common flux level, it becomes easy to visualise the spectral variations caused by the intense cometary activity around the star (see Fig. 1 for Fe II). However, to retrieve the absorption profile of a given exocomet, one needs to recover a reference stellar spectrum, free of any cometary absorption.

This Exocomet-Free Spectrum (EFS) is obtained using a method similar to the one described in Vrignaud et al. (2024a): First, we identify, for each spectrum, the set of lines affected by comet absorption, and the radial velocity ranges at which this absorption occurs (as an example, Table B.1 provides the ranges used for the strongest Fe II lines). We then average, for each wavelength pixel, all the spectra for which no comet absorption is expected (at that pixel).

This method was used for all lines, except for the 1850 Å Al III and 3900 Å Ca II doublets. In Al III, the comets studied in the following (which are also detected in Fe II, Ni II...) are often blended with wider, highly variable absorption features, barely seen in singly ionised species. We thus did not calculate any EFS for this doublet; instead, for each exocomet, a continuum was fitted on nearby spectral regions using a cubic spline algorithm, and used as a reference spectrum. For the HARPS observations of the Ca II doublet, we used the same method as introduced in Kiefer et al. (2014b), which takes advantage of the very high number of available observations of β Pic at these wavelengths (9 000+ HARPS spectra obtained from 2003 to 2024). Finally, for the MJUO data, we used the reference spectrum provided in Tobin et al. (2019).

A sample of spectral lines showing clear comet absorption is provided on Fig. C.1, along with the calculated EFS. For lines where very few observations are available, the recovery of the EFS might be incomplete (e.g. the Fe II 2399 Å line).

2.4. Correlation between cometary features

As pointed out in Vrignaud & Lecavelier des Etangs (2024), the cometary absorptions observed in Fe II lines correlate well with signatures observed in other species (Ni II, Cr II). As an example, Fig. 3 shows two observations of β Pic in Fe II (STIS) and Ca II (HARPS), obtained one hour apart on December 15, 2018. The similarity of the absorption features is striking; in particular, a strong redshifted comet (designated below as comet 18, see table D.1) is clearly visible in both spectra, roughly between 15 and 30 km/s.

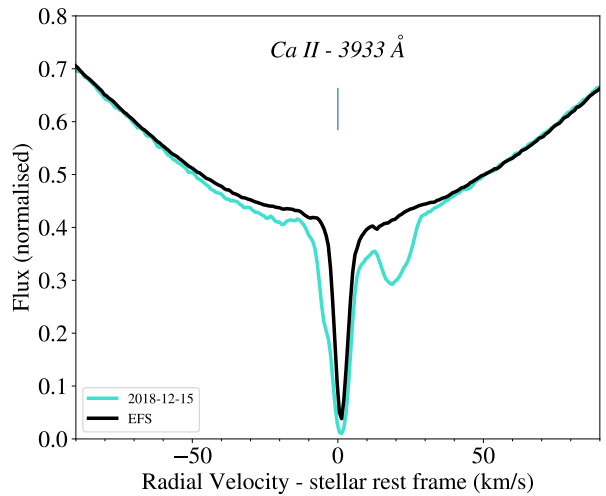
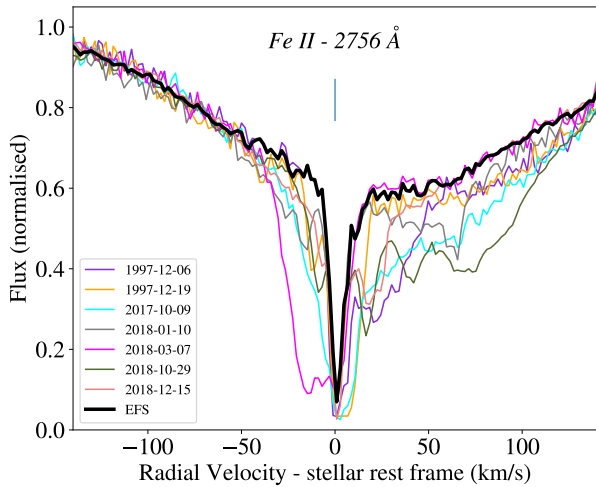
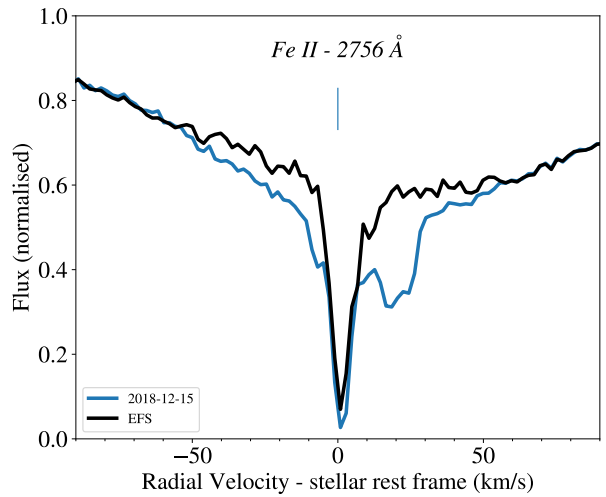
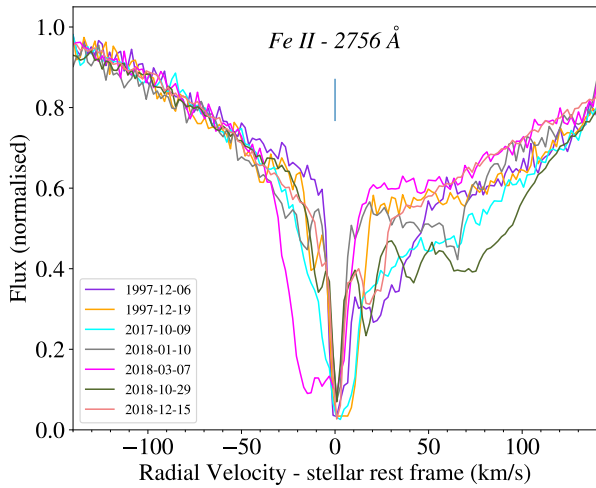


Fig. 1: Illustration of the EFS recovery. **Top**: 2728 Å Fe II line, showing clear spectral variations from one visit to another. **Bottom**: same line, showing the calculated EFS.

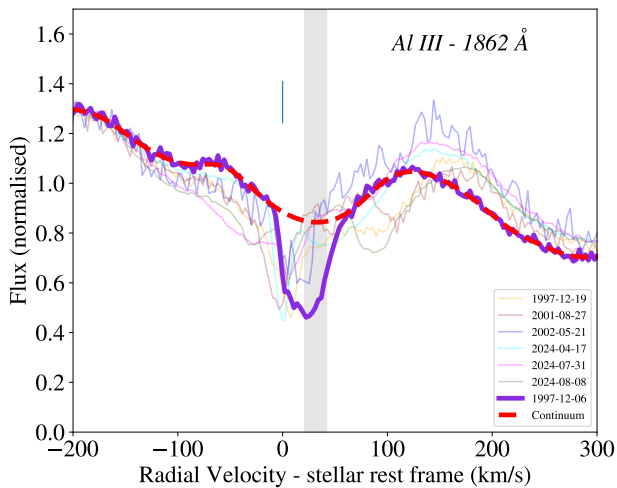


Fig. 2: Recovery of a reference spectrum for comet #1 (1997-12-06, grey area) in the Al III 1862 Å line. Contrary to other lines, we do not try to recover the EFS; instead, we fit a continuum to the observed spectrum using a cubic spline algorithm. This allows us to correct from the blending with other wide, shallow exocomets.

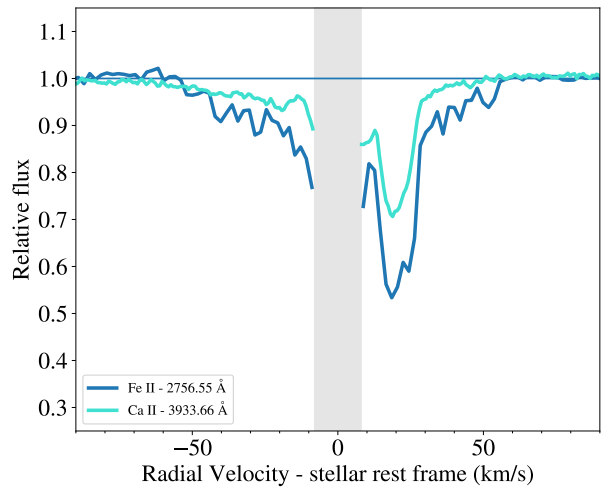


Fig. 3: Cometary absorption observed in Fe II (top) and Ca II lines (middle, one hour later) on December 15, 2018. The EFS is plotted with a thick black line. The comparison of the absorption after division by the reference spectrum is given in the bottom panel (the region near the circumstellar line was removed, due to a poorer EFS determination in Fe II lines).

The strong correlation between exocometary features observed in lines from different species shows that ions in exocometary tails usually stay mixed, thanks to efficient momentum exchange via Coulomb scattering (Vrignaud & Lecavelier

des Etangs 2024). This ion mixing is a key feature of β Pic exocomets, as it ensures that the signatures of a comet in a set of lines from different species are not influenced by the spatial distribution of each species individually, but rather by the comet geometry as a whole (e.g., covering factor), by the intrinsic spectral properties of each species (e.g., oscillator strengths), and by the global composition of the tail. Combined with the curve of growth approach, this ion mixing greatly facilitates the estimate of abundance ratios in β Pic exocomets.

3. A multi-species curve of growth model

3.1. The curve of growth approach

Introduced in Vrignaud et al. (2024a), the curve of growth approach aims at constraining the physical properties of a transiting exocomet observed in spectroscopy. Instead of focusing on a single spectral line, this approach relies on comparing the exocomet absorption depth in many (typically 10-100) lines, with diverse oscillator strengths and excitation levels. The dependency of the comet's absorption depth with the line oscillator strength and excitation energy can provide valuable estimates of the comet's physical properties (column density, excitation temperature, and size given by the covering factor of the stellar disk).

The study of Vrignaud et al. (2024a) presented a first curve of growth model, where a transiting comet is approximated by a cloud with an homogeneous column density, covering a limited fraction of the stellar disk, and characterised by a uniform excitation temperature. In this model, the average absorption depth $\overline{\text{abs}}_{lu}$ (see definition in Vrignaud et al. 2024a) of the comet in any line of a fixed species (such as Fe II) is given by:

$$\overline{\text{abs}}_{lu} = \overline{\alpha} \cdot (1 - e^{-\tau_{lu}}), \quad (1)$$

with $\tau_{lu} = \gamma \cdot \frac{\lambda_{lu}}{\lambda_0} g_l f_{lu} \cdot e^{-E_l/k_B T}$ the optical depth of the considered line. Here, l and u denote the lower and upper levels of the transition, and λ_{lu} , f_{lu} , g_l and E_l its wavelength, oscillator strength, lower level multiplicity, and lower level energy (respectively). The model is characterised by three parameters: $\overline{\alpha}$, the comet's average covering factor; γ , the typical optical thickness of the studied species (linked to its column density, see Sect. ?? below); and T , its excitation temperature. These parameters are, a priori, specific to the radial velocity range where the comet's average absorption depths are measured, and to the considered species (e.g., Fe II). Finally, λ_0 is an arbitrary wavelength. As in previous studies, we will use $\lambda_0 = 2756.551 \text{ \AA}$ (which is the wavelength of a strong Fe II line), regardless of the studied species.

Despite its simplicity, this one-zone model happens to fit most of the observed variable absorptions in β Pic spectrum well (see Sect. 4). However, Vrignaud & Lecavelier des Etangs (2024) noted that some cometary signatures can slightly deviate from this model, and are better described by the transit of several gaseous components with various sizes and optical depths.

Vrignaud & Lecavelier des Etangs (2024) thus introduced a more sophisticated curve of growth model, in which a transiting comet is represented with two gaseous components: a dense core and a surrounding, thinner envelope. This new model has now five parameters: $\overline{\alpha}_t$, the total comet's covering factor, $\overline{\alpha}_c$, the covering factor of the core component, γ_c , the typical optical thickness in the core component, γ_e/γ_c , the optical thickness ratio between the external and core components, and T , the excitation temperature throughout the comet. The average absorption depth $\overline{\text{abs}}_{lu}$ of the comet in any line of the studied species is now

expressed as:

$$\overline{\text{abs}}_{lu} = \overline{\alpha}_c \cdot (1 - e^{-\tau_{c,lu}}) + \overline{\alpha}_e \cdot (1 - e^{-\tau_{e,lu}}), \quad (2)$$

with:

$$\tau_{c,lu} = \gamma_c \cdot \frac{\lambda_{lu}}{\lambda_0} g_l f_{lu} e^{-E_l/k_B T},$$

$$\tau_{e,lu} = \gamma_e \cdot \frac{\lambda_{lu}}{\lambda_0} g_l f_{lu} e^{-E_l/k_B T},$$

and $\overline{\alpha}_e$ and γ_e the covering factor and typical optical thickness of the outer envelope, given by:

$$\begin{aligned} \overline{\alpha}_e &= \overline{\alpha}_t - \overline{\alpha}_c, \\ \gamma_e &= \gamma_c \cdot \frac{\gamma_e}{\gamma_c}. \end{aligned}$$

Again, the five model parameters are - a priori - specific to the studied species (Fe II, Ni II...) and to the radial velocity range where the comet's average absorption depth is measured.

3.2. Fitting several species simultaneously

In previous studies, these models were mostly applied to Fe II lines, which are very numerous and show strong comet absorption. However, Vrignaud et al. (2024a) showed that the absorption signatures of individual exocomets in lines from different species (Ni II, Cr II) tend to have the same shape and to follow the same curve of growth as Fe II; in other words, the comet geometry ($\overline{\alpha}$, $\overline{\alpha}_c$...) and excitation temperature (T) constrained by Fe II lines also apply to other species.

In the following, we will thus assume that exocometary gaseous tails always remain well-mixed, regardless of their overall shape. This hypothesis allows us to introduce a multi-species curve of growth model, able to fit several species simultaneously. Going back to Eq. 1 and 2, we now assume that the geometric parameters ($\overline{\alpha}$ for Eq. 1, $\overline{\alpha}_t$, $\overline{\alpha}_c$, γ_e/γ_c for Eq. 2) and the excitation temperature (T) are the same for all species; only the γ (Eq. 1) and γ_c (Eq. 2) parameters remain specific to each atom or ion. These assumptions allow us to refine Eqs. 1 and 2 into Eqs. 3 and 4:

$$\overline{\text{abs}}_{lu, i} = \overline{\alpha} \cdot (1 - e^{-\tau_{lu, i}}) \quad (3)$$

with:

$$\tau_{lu, i} = \gamma_i \cdot \frac{\lambda_{lu}}{\lambda_0} g_l f_{lu} \cdot e^{-E_l/k_B T},$$

and:

$$\overline{\text{abs}}_{lu, i} = \overline{\alpha}_c \cdot (1 - e^{-\tau_{c,lu, i}}) + \overline{\alpha}_e \cdot (1 - e^{-\tau_{e,lu, i}}) \quad (4)$$

with:

$$\tau_{c,lu, i} = \gamma_{c, i} \cdot \frac{\lambda_{lu}}{\lambda_0} g_l f_{lu} e^{-E_l/k_B T},$$

$$\tau_{e,lu, i} = \gamma_{c, i} \cdot \frac{\gamma_e}{\gamma_c} \cdot \frac{\lambda_{lu}}{\lambda_0} g_l f_{lu} e^{-E_l/k_B T}.$$

In the above equations, we now use a letter i to specify the species associated with the line (l, u). The two models have now respectively $n + 2$ and $n + 4$ parameters, with n the number of fitted species.

3.3. Estimating abundance ratios

Equations 3 and 4 can be fitted to the absorption depths of a given comet in a set of lines from several species, in order to constrain the comet geometry, excitation temperature, and typical optical thicknesses of each species (γ_i for Eq. 3, $\gamma_{c,i}$ for Eq. 4). Once constrained, these parameters allow for the estimate of the total column density of each species, through (see Vrignaud et al. 2024a; Vrignaud & Lecavelier des Etangs 2024):

$$N_{\text{tot},i} = \frac{4\varepsilon_0 m_e c}{e^2 \lambda_0} \Delta v Z_i(T) \gamma_i \bar{\alpha}$$

for the one-zone model (Eq. 3), and:

$$N_{\text{tot},i} = \frac{4\varepsilon_0 m_e c}{e^2 \lambda_0} \Delta v Z_i(T) \gamma_{c,i} (\bar{\alpha}_c + (\gamma_e/\gamma_c) \bar{\alpha}_e)$$

for the two-component model (Eq. 4). Here, Δv is the radial velocity width of the comet, $Z_i(T)$ is the partition function of the considered species, and ε_0 , m_e , and c are respectively the vacuum permittivity, electron mass and light velocity. Using the assumption that the geometric parameters are identical for all the studied species, the abundance ratio of two species i, j then writes:

$$\left[\frac{i}{j} \right] = \frac{N_{\text{tot},i}}{N_{\text{tot},j}} = \frac{Z_i(T) \gamma_i}{Z_j(T) \gamma_j}, \quad (5)$$

where the γ_i and γ_j parameters are replaced by $\gamma_{c,i}$ and $\gamma_{c,j}$ in the case of a two-component model.

4. Application to a sample of comets

4.1. The sample of exocomets

Our study aims at measuring the abundance ratio of several atoms and ions (S I, Fe II, Ni II...) in β Pic exocomets, using the available spectroscopic data. To carry out this analysis, we selected a set of 29 comets that appear to be well suited for abundance measurement. All these comets produce significant, well-individualised absorption in a large number of Fe II lines (used as a reference species), as well as in, at least, one other refractory species (Cr II, Ni II, Ca II...). Basic information on the 29 selected comets is provided in Tab. D.1. A unique identifier was attributed to each object (e.g., " β Pic C19971206 a" for comet 1), according to the upcoming nomenclature of Lecavelier des Etangs et al. (in prep). A snapshot of each comet in one strong Fe II line is also provided in Fig. E.1.

4.2. Studied species and line selection

Throughout our cometary sample, we were able to probe a total of 12 refractory species, listed in Table 1, reflecting most of the abundant exocometary species with optically-allowed spectral lines in the UV/visible. Most of the studied species are ions, except for S I, which stands out by its fairly high ionisation potential compared to most neutral species (10.36 eV). Other atoms (Fe I, Mg I, Si I, Ca I...) with lower ionisation potentials (≤ 8 eV) were not detected in any exocomet, and thus not included in the study. This non-detection is probably the result of efficient photo-ionisation. Despite noticeable spectral variations, Al II, Si III and Si IV were also not included in the study, due to a very poor Signal-to-noise ratio (S/N) in the 1670 Å Al II and 1206 Å Si III lines, and to highly blended absorption in the 1400 Å Si IV doublet.

For each individual exocomet, it was never possible to probe the abundance of all 12 species simultaneously, either because the appropriate lines were not observed, or because the lines were too faint or too saturated to be exploited. As an example, the Cr II/Fe II could be constrained only for the strongest comets (typically when $N_{\text{tot,Fe II}}/\Delta v > 10^{13} \text{ cm}^{-2}/\text{km s}^{-1}$), as cometary signatures in Cr II are usually very faint (a few % at most). On the other hand, the Mg II/Fe II ratio was estimated only for the faintest comets ($N_{\text{tot,Fe II}}/\Delta v \sim 10^{12} \text{ cm}^{-2}/\text{km s}^{-1}$), as Mg II signatures are easily saturated.

The set of lines used to fit each exocomet was selected carefully. In particular, we did not include lines blended in close multiplets (i.e., when the lines separation is lower than the typical width of cometary signatures; see for instance Fig. 4). Lines for which the S/N on the cometary absorption depth is below unity were also not included in the fit, as well as those showing spurious features. Finally, we removed the lines for which no reliable EFS can be determined, generally due to an insufficient number of observations. The complete list of lines used throughout the study is given in Table G.1. Most of the line parameters (λ_{lu} , A_{ul} , ...) were obtained from the NIST database (Kramida et al. 2023). Table D.1 also provides, for each comet, the list of line series considered in the fit.

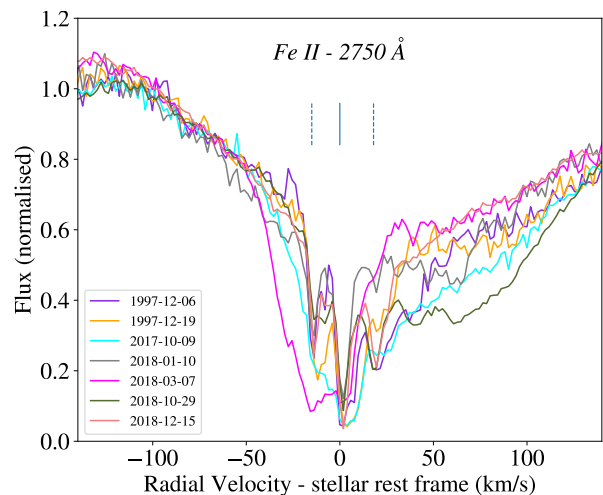


Fig. 4: Zoomed-in view of the 2750.13 Å Fe II line (indicated with a solid, blue marker). Even if cometary signatures are detected, they are blended with absorptions from other close Fe II lines, at 2749.99 and 2750.30 Å (dotted markers). Due to this blending, the triplet was not included in our curve of growth analysis.

4.3. Fit procedure

Each comet was fitted using a similar procedure:

- We first measured the average absorption depth (relative to the EFS) of each comet in each line of its selected set. As in Vrignaud et al. (2024a), uncertainties on absorption measurements were estimated by taking into account photon noise (generally between 0.5 and 3%) and systematic errors due to imperfect flux calibration (0.5–1%, estimated by comparing our spectra on stable spectral domains). For each comet, the RV range used to measure its absorption depth was chosen as the range where the absorption is the deepest, to limit the impact of systematic uncertainties. The RV ranges used in the fits are provided in Table D.1.

Table 1: List of the studied chemical species sorted by ionisation energy.

Species	S I	Ca II	Mg II	Mn II	Fe II	Si II	Cr II	Co II	Zn II	Ni II	S II	Al III
Ionisation energy (eV)	10.36	11.87	15.04	15.64	16.19	16.35	16.49	17.08	17.96	18.17	23.34	28.45

- We then fitted the measured absorption depths of each comet using one of the multi-species curve of growth models (Eq. 3 or 4) and a MCMC algorithm from the emcee python library (Foreman-Mackey et al. 2013). These fits provided constraints on the geometry and excitation temperature of each comet, as well as on the γ values of each fitted species.
- We finally estimated the abundance of each fitted species, using Eq. 5. To properly estimate uncertainties, this ratio is calculated at each step of the Markov chains.

Comets 22-29 (HST program #17421) were all observed during a rather long time (3-4 HST orbits), enough to observe variation in their absorption profile. Each of these comets was analysed once, using the HST orbit showing the more individualised and deep absorption (e.g. for comet #22, the second orbit of the 2024-04-17 visit). The specific HST orbits used for these comets are provided in Table D.1.

The one-zone curve of growth model was used for most comets, as it generally provides satisfactory fits. The only exceptions are comets #1, #2 and #6, which appeared to be significantly better fitted with a two-component model (based on the comparison of the Bayesian Information Criteria (BIC) of the two models).

For comets observed in a set of Fe II lines covering a wide energy range (E/k_b typically in the range 0 – 12000 K), the excitation temperature was set as a free parameter. For other comets, we used a Gaussian prior ($T = 9000 \pm 500$ K), based on values found for exocomets where the excitation temperature could be directly measured. This prior enabled us to estimate column densities in all exocomets, even those for which no direct estimate of the excitation temperature could be performed.

4.4. Results

The curves of growth of the fitted comets are shown on Fig. E.1. The physical properties of the comets (covering factor, total Fe II column density, excitation temperature) and their measured compositions (abundance ratios) are provided in Table F.1 and F.2, respectively. All abundance ratios are expressed relatively to Fe II, which serves as a reference species. A visual recapitulation of all abundances measurements is also provided in Fig. 5, allowing to visualise the dispersion of each species.

5. Discussion

5.1. Excitation temperatures

Before digging into the composition of our cometary sample, it is interesting to look at the temperatures that has been measured in comets #1 to #6 and #8 (Table F.1). In all these cases, the excitation temperature of the transiting comets remains close to 9000 K. This result validates the conclusion of Vrignaud & Lecavelier des Etangs (2024), which studied in details the excitation state of Fe II in comet #1: the density in the gaseous cloud surrounding the exocomets is generally sufficiently low for the gas excitation to be controlled by the stellar flux rather than by electronic collisions (radiative regime). In this context, the excitation temperature of the gas is roughly set to the stellar effective

temperature (~ 8052 K, Gray et al. 2006). The slight discrepancy observed between the typical excitation temperature found in exocomets (~ 9000 K) and the stellar effective temperature could be explained by the presence of absorption lines in the stellar spectrum (as proposed for solar system comets, Manfroid et al. 2021) or by the self-opacity of the transiting gas, which distorts the stellar spectrum received in the innermost regions of the transiting comets.

This consistency of excitation temperature led us to assume that all β Pic exocomets follow a radiative regime, even those for which the gas excitation cannot be directly probed because of an insufficient wavelength coverage. For these comets, we thus applied a gaussian prior on T of 9000 ± 500 K, based on the values found for comets 1-6 and 8 (particularly comets 1, 4, 5 and 8, for which the most accurate values of T could be obtained).

5.2. Ion abundance

The abundances of most of the singly ionised species (Ca II, Ni II, Si II, Cr II, Mn II, Mg II) relative to Fe II appear to be fairly consistent throughout our cometary sample, with values typically spanning over a factor 2-3 at most. As an example, the measured Ca II/Fe II ratio spans from 3×10^{-3} to 8×10^{-3} (mean: 5.8×10^{-3}), the Ni II/Fe II ratio from 5×10^{-2} to 10×10^{-2} (mean: 7.6×10^{-2}), and the Si II/Fe II ratio from 0.7 to 1.5 (mean: 0.95). For Ca II, the spread of abundance measurements is wider than the typical uncertainty on each measurement, indicating that the Ca II/Fe II ratio can vary slightly from one comet to another, up to a factor of ~ 3 . The origin of this diversity is however unclear; no correlation of the Ca II/Fe II ratio with radial velocity is observed (Fig. 6), which could have been expected given that low-velocity and high-velocity comets usually belong to two separated families with different transit distance (Kiefer et al. 2014b). For Ni II, Si II, Cr II, Mn II and Mg II, the observed abundance distributions are consistent with the estimated error bars; it is therefore difficult to conclude on any diversity in the composition of our comet sample. In addition, the abundance of these species does not seem to be correlated with radial velocity.

A few species, however, exhibit a much wider abundance distribution (Fig. 5). The most obvious one is Al III, with a Al III/Fe II ratio spanning a factor of 20 and ranging from ~ 0.01 (comets #5, #21) to 0.2 (comet #6). The Al III abundance is found to be strongly correlated with redshift: the most redshifted comets are usually those who exhibit the strongest Al III absorptions (Fig. 7). The S I abundance in β Pic exocomets also seems fairly diverse: this atom is clearly detected in comets #5 and #21 ($S I/Fe II \sim 9 \cdot 10^{-3}$, see Table F.2), but barely noticed in comets #1 and #20 (abundance measurements for other comets were not included in the study, due to much larger uncertainties). Here, it is interesting to note that the only two comets found to harbour a significant amount of S I are those who display the weakest Al III signatures (Fig. 7): contrary to Al III, the S I abundance in β Pic exocomets seems to be anti-correlated with redshift, with low-velocity comets showing higher S I/Fe II ratio. These correlations (or anti-correlations) are very likely linked to the transit distance of the comets: highly redshifted comets are generally closer to the star, meaning that they receive a greater irradiation.

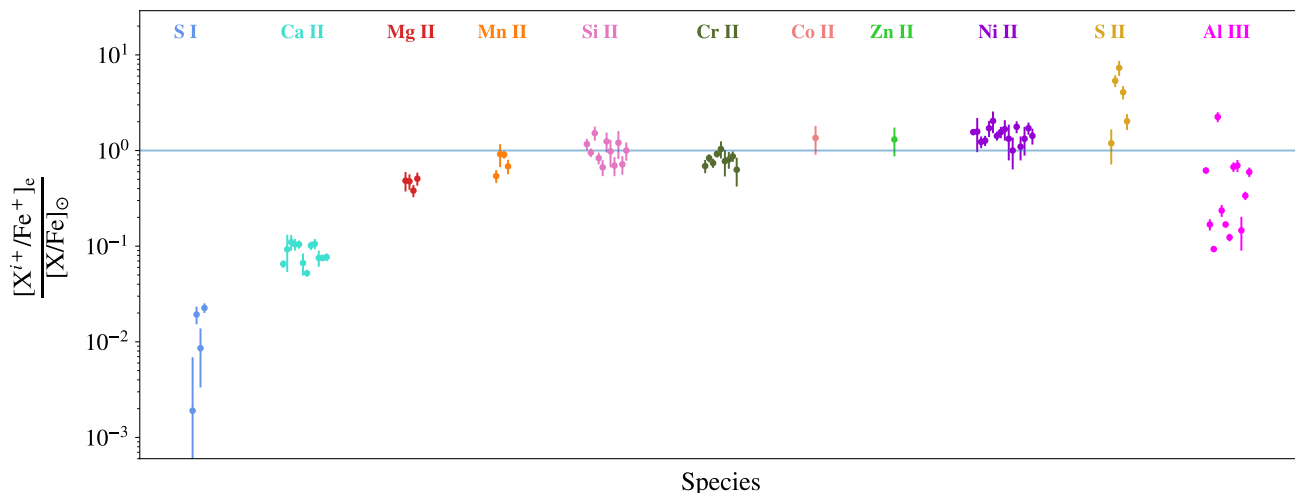


Fig. 5: Overview of all abundance measurements performed throughout the 29 exocomet sample, grouped by chemical species. For each species (e.g. S I), the measured ratios with Fe II were divided by the solar ratio of the corresponding elements (e.g. S/Fe), as given by Asplund et al. (2009). The ordering of the species reflect their ionisation energy; each group of measurements is ordered according to the comet indexes (Tab. D.1).

According to the model proposed in Beust & Tagger (1993), this would lead to a higher ionisation degree in cometary gas, due to a denser and hotter bow shock at the front of the coma. On the contrary, some low-redshift comets appear to be sufficiently far away from the star to allow S I to survive ionisation (and prevent the formation of large amounts of Al III), indicating that the compression mechanisms in their comae are much softer.

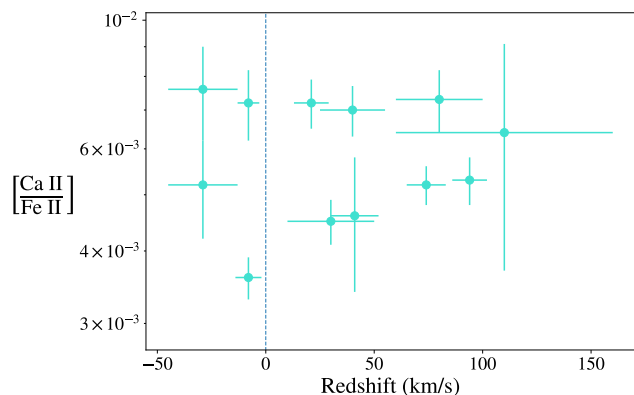


Fig. 6: All Ca II/Fe II ratios measured in our exocometary sample, as a function of the comet redshift. Horizontal error bars reflect the radial velocity extent of the cometary signatures.

Finally, important variations were found for the S II/Fe II ratio (estimated in five exocomets; see Fig. 5), with values ranging from 0.5 to 3. However, these measurements should be taken with cautious: Fe II and S II are observed with two different HST instruments (STIS and COS), at different resolutions, and during separate HST orbits, necessarily separated by 96 minutes. Further observations may thus be needed to confirm this diversity in S II/Fe II ratios. For Co II and Zn II, only comet #1 (1997-12-06) could provide constraints on their abundances, with rather large uncertainties. It is therefore impossible to characterise the diversity of exocomet composition regarding these two species.

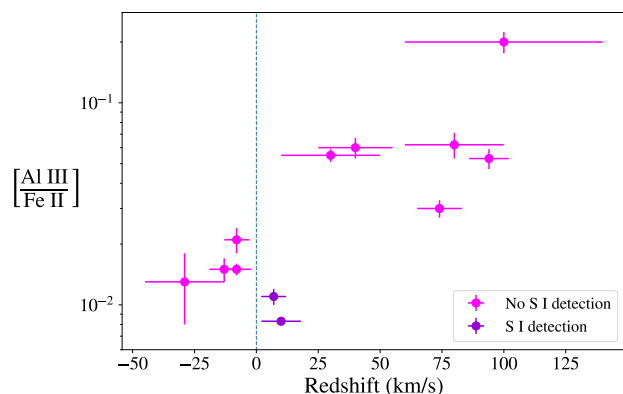


Fig. 7: All Al III/Fe II ratios measured in our cometary sample, as a function of the comet redshift. Horizontal error bars reflect the radial velocity extent of the cometary signatures. The two violet markers indicate the two comets with clear S I detections (see text).

5.3. Link between abundances and ionisation energies

Figure 5 shows that the typical abundances of the studied species in β Pic exocomets are generally consistent with solar abundances. For instance, the exocometary Si II/Fe II ratio is close to the solar Si/Fe ratio, ≈ 1 . These quasi-solar values hint that the first ionisation degree is probably a major form of the studied elements. However, we also note some discrepancies: S I, Ca II and Mg II appear to be always depleted (by factors of ~ 100 , 10 and 2, respectively), while Ni II and S II seem to be over-abundant (by a factor 1.5 for Ni II, and 2 to 6 for S II).

To understand this trend, it is useful to plot the average abundances (normalised to the solar values) as a function of their ionisation potentials (Fig. 8; see the numerical values in Table 2). A clear correlation is visible: the more difficult to ionise a species is, the more abundant it is in β Pic exocomets. The observed deviations from solar ratios are thus probably due to a diversity of ionisation states among the studied species. For instance, the depletion of Ca II is probably due to the higher ionisation degree of Ca than other species, as Ca II is much more easily ionised into Ca III (11.87 eV, Table 1) than Fe II into Fe III or Ni II into Ni III

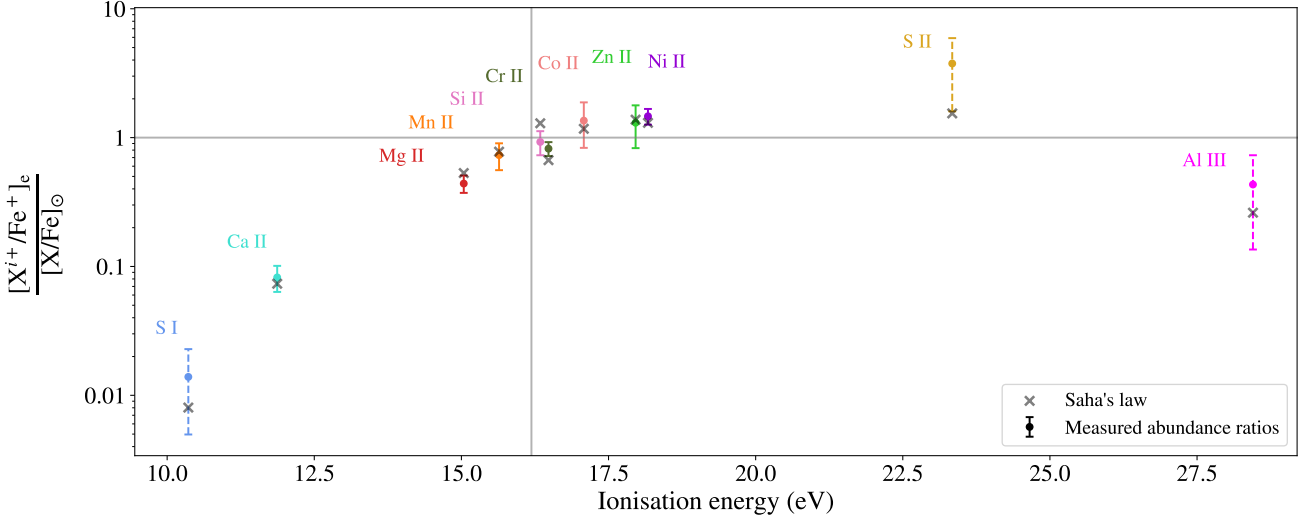


Fig. 8: Typical abundances of 11 atom and ions in β Pic exocomets, relative to Fe II and normalised by solar abundances. The numerical values used to build this figures are provided in Tab. 2. Grey crosses indicate the best-fit model with Saha’s equation (see Sect. 5.4.2).

(note that, for all these species, the neutral fraction is negligible, due to photo-ionisation). Similarly, the high ratio of S II/Fe II compared to the solar S/Fe ratio is likely caused by the very dif-

ficult ionisation of S II into S III (23.34 eV), which leads a higher fraction of sulphur to remain as S⁺ in the cometary tails.

In between, the nearly solar ratios found for Mn II, Si II and Cr II relatively to Fe II are consistent with these four species having similar ionisation energies (~ 16 eV). These solar ratios suggest that the dust sublimation is efficient enough for the composition of the gaseous tail to reflect the dust composition itself, which is probably solar for refractory elements. This result is very different from solar system comets, for which the composition of the gas is primarily influenced by the varying sublimation rates of the cometary materials. For instance, in some solar system comets the Ni/Fe ratio has been found to be strongly super-solar (Manfroid et al. 2021), due to faster sublimation rates for nickel carbonyls (e.g. Ni(CO)₄) compared to iron carbonyls (e.g. Fe(CO)₅).

The Al III/Fe II ratio is slightly more difficult to interpret, since Al III is ionised twice: a significant fraction of Al is probably retained as Al II, while, for neutral or singly ionised species (S I, Ca II...), the fraction in lower ionisation states is either null or negligible. This explains why the Al III/Fe II ratio is generally sub-solar, even if Al III is very difficult to ionise (28.4 eV).

Table 2: Average abundances of 11 refractory species in β Pic exocomets, compared to solar ratios.

X^{i+}	$[X^{i+}/Fe^{+}]_e$	$[X/Fe]_{\odot}^a$	$\eta_X = \frac{[X^{i+}/Fe^{+}]_e}{[X/Fe]_{\odot}}$
S ⁰	5.8 ± 3.7 ($\cdot 10^{-3}$)	420 ± 50 ($\cdot 10^{-3}$)	0.014 ± 0.009^b
Ca ⁺	0.57 ± 0.11 ($\cdot 10^{-2}$)	6.9 ± 0.9 ($\cdot 10^{-2}$)	0.082 ± 0.19
Mg ⁺	0.55 ± 0.05	1.26 ± 0.16	0.43 ± 0.07
Mn ⁺	6.2 ± 1.2 ($\cdot 10^{-3}$)	8.5 ± 1.1 ($\cdot 10^{-3}$)	0.73 ± 0.17
Si ⁺	0.95 ± 0.17	1.02 ± 0.12	0.93 ± 0.19
Cr ⁺	1.13 ± 0.05 ($\cdot 10^{-2}$)	1.38 ± 0.16 ($\cdot 10^{-2}$)	0.82 ± 0.10
Co ⁺	4.1 ± 1.4 ($\cdot 10^{-3}$)	3.1 ± 0.6 ($\cdot 10^{-3}$)	1.35 ± 0.52
Zn ⁺	1.5 ± 0.5 ($\cdot 10^{-3}$)	1.15 ± 0.17 ($\cdot 10^{-3}$)	1.30 ± 0.47
Ni ⁺	7.61 ± 0.28 ($\cdot 10^{-2}$)	5.2 ± 0.7 ($\cdot 10^{-2}$)	1.46 ± 0.20
S ⁺	1.58 ± 0.90	0.42 ± 0.05	3.8 ± 2.1
Al ²⁺	3.9 ± 2.6 ($\cdot 10^{-2}$)	8.9 ± 1.0 ($\cdot 10^{-2}$)	0.43 ± 0.29

^a (taken from Asplund et al. 2009).

^a Error bars on $[X^{i+}/Fe^{+}]_e$ reflect both the uncertainties on our measurements, and their dispersion around their average value.

5.4. The ionisation state

5.4.1. Using the Al III/Fe II ratio

The Al III/Fe II ratios can be used as probes of their ionisation states. Let us consider a given exocomet, and some chemical element X (e.g. Fe, Ca...). Assuming that the $[X/Fe]$ and $[Al/Fe]$ ratios in the studied exocomet are solar, the $[X_{II}/X]$ ratio can be written as (see App. A):

$$\left[\frac{X_{II}}{X} \right]_e = \left(\frac{\eta_{Al}}{\eta_X} + \frac{1}{\eta_X s_{Al}} \left[\frac{Al_{III}}{Fe_{II}} \right]_e \right)^{-1}, \quad (6)$$

with:

$$s_{Al} = [Al/Fe]_{\odot},$$

$$\eta_X = \frac{[X_{II}/Fe_{II}]_e}{[X/Fe]_{\odot}}, \quad \eta_{Al} = \frac{[Al_{II}/Fe_{II}]_e}{[Al/Fe]_{\odot}},$$

where the index e denotes ratios in the considered exocomet and η_X is the abundance of the single ionized state of the species X relative to Fe II in solar units.

Our study showed that the abundances of singly ionised species (Ca II , Cr II , Ni II ...) relative to Fe II in β Pic exocomets are fairly stable. We can thus make the assumption that η_X and η_{Al} are fixed parameters, independent of the considered exocomet. The value of η_X can be estimated from our measurements (e.g. $\eta_{\text{Ca}} = 0.082 \pm 0.019$, $\eta_{\text{Fe}} = 1$, $\eta_{\text{Ni}} = 1.46 \pm 0.20$; Table 2). However, the $\text{Al II}/\text{Fe II}$ ratios of the studied exocomets could not be measured due to the very low stellar flux in the $\text{Al II } 1670 \text{ \AA}$ line, preventing us from directly estimating η_{Al} . To mitigate this problem, we can note that the η value of a given element is primarily controlled by its ionisation potential (Fig. 8). Since the ionisation potential of Al^+ (18.8 eV) is rather close to that of Ni^+ (18.2 eV), we assume that $\eta_{\text{Al}} \approx \eta_{\text{Ni}} = 1.46$. We will thus assume in the following $\eta_{\text{Al}} = 1.5 \pm 0.3$.

Under these assumptions, Eq. 6 provides a direct link between the $\text{Al III}/\text{Fe II}$ ratio of a given exocomet and its $X \text{ II}/X$ ratio, provided that the η value of X can be constrained. For instance, Fig. A.1 provides estimates of the $\text{Ca II}/\text{Ca}$, $\text{Fe II}/\text{Fe}$ and $\text{Al II}/\text{Al}$ ratios of the comets for which the $\text{Al III}/\text{Fe II}$ ratio could be measured, using the η values given in Table 2. These three elements appear to have contrasted ionisation states: while most of Calcium is ionised at least twice ($\text{Ca II}/\text{Ca} \sim 0.04$), about half of iron remains singly-ionised ($\text{Fe II}/\text{Fe} \sim 0.5$), as well as most of aluminium ($\text{Al II}/\text{Al} \sim 0.6 - 0.9$). Overall, the ionisation state among the studied exocomets appears to be rather stable, with only a slightly larger fraction of Al being doubly-ionised in the most redshifted comets.

5.4.2. Using the Saha equation

The measured cometary abundances corrected from solar composition (Fig. 8) can also be fitted using Saha's law. This law writes, for any element X :

$$\left[\frac{X^{(i+1)+}}{X^{i+}} \right] = \frac{2}{n_e \Lambda(T)^3} \frac{Z_{X^{(i+1)+}}(T)}{Z_{X^{i+}}(T)} \exp\left(-\frac{E_{i+1}}{k_B T}\right), \quad (7)$$

with $\Lambda(T) = \sqrt{\frac{h^2}{2\pi m_e k_B T}}$. The parameters of this law are T , the electronic temperature in the ionisation region, and n_e , the electronic density.

The typical composition of β Pic exocomets appears to match rather well this simple law (see the grey crosses in Fig. 8). The fitted temperature is $T = 12\,200 \pm 300 \text{ K}$, which may be considered as the typical temperature in the ionising part of β Pic exocomets. However, to fit the measurements with the Saha's law, the leading factor in Eq. 7 yields an equivalent electronic density of $\log(n_e \text{ (cm}^{-3}\text{)}) = 21.33 \pm 0.16$, which is, of course, much too large to be realistic (geometric estimate provide values in the range $10^5 - 10^6 \text{ cm}^{-3}$, Vrignaud & Lecavelier des Etangs 2024). Saha's equation is thus probably not the right tool for modelling the ionisation mechanisms in β Pic exocomets: a complete description of the ionisation and recombination rates is probably needed to fully understand these mechanisms.

Nevertheless, our fit provides a first quantitative description of the ionisation state in β Pic exocomets. For instance, Fig. 9 shows the ionisation distributions of a few elements, as constrained by Saha's law. While Fe, Mg and Al appear to be split in similar fractions between their singly and doubly ionised forms, Ca is, for the most part, doubly ionised. This is fully consistent

with direct estimates from Sect. 5.4.1. With the constrained parameters (T , n_e), one can also predict the expected ionisation state of other elements. For instance, the main form of C in β Pic exocomets should be C II (Fig. 9), with only a small fraction in neutral form (about 1-2%). However, C IV (also detected in β Pic exocomets, Deleuil et al. 1993; Vidal-Madjar et al. 1994) is not produced in the model, showing that this first description of the ionisation state in β Pic exocomets is perfectible and other mechanisms should play an important role (see, for instance, Beust & Tagger 1993).

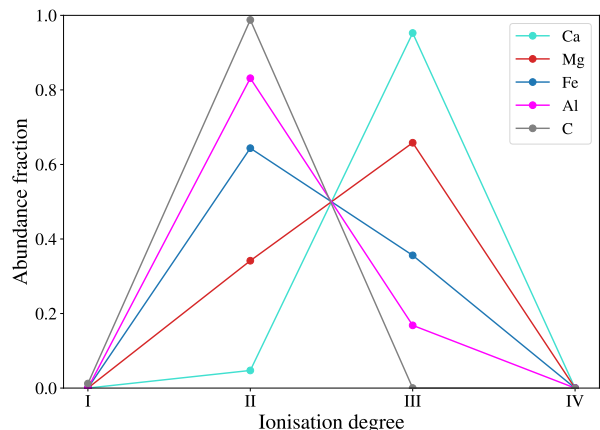


Fig. 9: Typical ionisation state of five elements in β Pic exocomets, as constrained by the fit of our abundances measurements (Fig. 8) with Saha's equation.

Finally, the dispersion of $\text{Al III}/\text{Fe II}$ ratios in the cometary sample can be fairly well reproduced by Saha's equation, by letting T vary from 10 800 K (comets 5 and 21, with the lowest $\text{Fe II}/\text{Al III}$ ratio) to 14 900 K (comet 6, showing the highest ratio). It thus appears that the physical conditions in the ionising tails of the studied exocomets are rather uniform, despite the apparent diversity of these objects (e.g., they cover a wide range of redshift and line width).

5.5. Limitations

The main limitation of our abundance measurements is that they are very fragmented: even though the number of studied species is rather large (12, including Fe II), these species were never observed altogether in one individual exocomet. In fact, most of the studied comets are generally observed in less than 5 different species simultaneously. This considerably limits our ability to study the variety of composition and ionisation states among β Pic exocomets, as we are still unable to build diagrams similar to Fig. 8 but for individual comets. In Sect. 5.4.2, Saha's equation was thus fitted to the average abundance ratios measured across our comet sample (Table 2), providing rough constraints on the typical ionisation state of β Pic exocomets rather than on the properties of any individual object.

Some of our abundances measurements should also be taken with caution, due to observing limitations. This is in particular the case for abundance ratios derived from non-simultaneous observations (e.g. the $\text{Ca II}/\text{Fe II}$ ratios), which may be affected by time-variation of the total amount of gas transiting the star. The different spectral resolutions of COS ($R = 16\,000 - 24\,000$) and STIS ($R = 115\,000$) also make the estimate of the $\text{S II}/\text{Fe II}$ ratio slightly hazardous, as the cometary features observed in S II (with COS) are often blended. The curve of growth approach

may thus not be the best tool to study exocomet absorption in S II; here a complete modelling of the cometary profile may be required.

It should also be noted that the assumption that the gas follows a Boltzmann distribution at $T \sim 9000$ K may not be valid for all the studied species. In particular, due to the very low stellar flux in the bottom of the Ca II H&K lines, the excitation of Ca II in the transiting comets may be fairly different than assumed by our model. Modelling the level population of Ca II in a similar way to that of Vrignaud & Lecavelier des Etangs (2024) and using radiative and collision coefficients from Meléndez et al. (2007), we calculated that $\sim 87\%$ of Ca II should remain in its ground state, compared to $\sim 62\%$ if the gas follows a Boltzmann distribution at 9000 K. Since our measurements are based on observations of the ground state of Ca II (through the H&K lines), the Ca II/Fe II ratios of the studied exocomets might be overestimated by as much as $\sim 40\%$. Although the case of Ca II is probably special due to the extreme depth of the photospheric H&K lines, abundance measurements in other species may also be biased for this reason. Overcoming this issue would require a complete modelling of the energy distribution of all the studied species, which is beyond the scope of the present work.

6. Conclusion

Our study provided the first abundance measurements of 12 ionised species in a large sample of exocomets that transited β Pic between 1997 and 2024. We found that the composition of the gaseous tails is fairly stable from one comet to another, particularly for singly-ionised species (Ca II, Ni II, Cr II...), and overall consistent with solar abundances. This validates the use of the curve of growth approach to study the composition of β Pic exocometary tails.

We also showed that the typical abundances of refractory ions in β Pic exocomets is strongly correlated with ionisation energy, hinting that ionisation is playing a prominent role in the composition of these gaseous tails. For instance, Ca II, fairly easy to ionise (11.9 eV), is systematically depleted by a factor ~ 10 compared to Fe II (16.2 eV). A closer study of the measured abundances showed that Fe is generally split in similar fraction between Fe II and Fe III, while only $\sim 4\%$ of Ca is in the form of Ca II, the rest being Ca III. These estimates were confirmed by the fit of our abundance measurements with the Saha equation. A clear correlation between the Al III/Fe II ratio and the radial velocity was also noted, showing that the most redshifted comets are generally more ionised, likely due to their closer distance to β Pic. These results could enable further studies of the ionization processes in β Pic exocomets, in order to quantify the relative contributions of potential mechanisms such as photoionization, electron impact ionization, or stellar wind charge exchange.

This first characterization of the typical ionization state in β Pic exocomets now allows us to predict the ionisation state of other elements, including tracers of volatiles (C, N, O). For instance, extrapolating the fitted Saha's law to carbon, we can estimate that the typical neutral fraction of C in β Pic exocomets is around 1-2 %. This value, coupled with observations of exocomets in C I and Fe II lines (both accessible with STIS), could enable the determination of the C/Fe ratio of β Pic exocomets, yielding valuable insight into their formation mechanisms.

However, our abundance measurements remain fragmented: the number of detected species in each individual comet is generally too low to allow a case-by-case study of their ionisation state and composition. To overcome this lack, new observations of β Pic on a broader wavelength domain are required, to allow

the detection of new exocomets in a large number of species simultaneously. Such observations will be obtained by 2025 with HST program #17790 (Vrignaud et al. 2024b), which will target the whole wavelength domain between 1200 and 2900 Å at four different epochs. This program will allow in-depth studies of the ionisation state in individual comets, thanks to simultaneous observations in a large number of species with diverse ionisation potentials (S I, Fe II, Ni II, S II, Mg II...). The C/Fe of the detected exocomets will also be inferred, using measurements in C I and Fe II lines and estimates of the ionisation state in each object. The present paper thus serves as a benchmark for these future studies, demonstrating the relevance of abundance ratios measurements to probe the composition of β Pic exocomets and identify the physical processes that ionize the gas.

Acknowledgements. T.V. & A.L. acknowledge funding from the Centre National d'Études Spatiales (CNES).

References

- Apai, D., Schneider, G., Grady, C. A., et al. 2015, *ApJ*, 800, 136
 Asplund, M., Grevesse, N., Sauval, A. J., & Scott, P. 2009, *ARA&A*, 47, 481
 Bergeson, S. D. & Lawler, J. E. 1993, *ApJ*, 414, L137
 Beust, H., Milli, J., Morbidelli, A., et al. 2024, *A&A*, 683, A89
 Beust, H. & Morbidelli, A. 1996, *Icarus*, 120, 358
 Beust, H. & Tagger, M. 1993, *Icarus*, 106, 42
 Boissé, P. & Bergeron, J. 2019, *A&A*, 622, A140
 Chen, C. H., Lu, C. X., Worthen, K., et al. 2024, *ApJ*, 973, 139
 Deleuil, M., Gry, C., Lagrange-Henri, A. M., et al. 1993, *A&A*, 267, 187
 Ferlet, R., Hobbs, L. M., & Vidal-Madjar, A. 1987, *A&A*, 185, 267
 Foreman-Mackey, D., Hogg, D. W., Lang, D., & Goodman, J. 2013, *PASP*, 125, 306
 Gontcharov, G. A. 2007, *VizieR Online Data Catalog*, III/252
 Gray, R. O., Corbally, C. J., Garrison, R. F., et al. 2006, *AJ*, 132, 161
 Kiefer, F., Lecavelier des Etangs, A., Augereau, J. C., et al. 2014a, *A&A*, 561, L10
 Kiefer, F., Lecavelier des Etangs, A., Boissier, J., et al. 2014b, *Nature*, 514, 462
 Kramida, A., Yu. Ralchenko, Reader, J., & and NIST ASD Team. 2023, *NIST Atomic Spectra Database* (ver. 5.11), [Online]. Available: <https://physics.nist.gov/asd> [2023, December 15]. National Institute of Standards and Technology, Gaithersburg, MD.
 Lagrange, A. M., Bonnefoy, M., Chauvin, G., et al. 2010, *Science*, 329, 57
 Lagrange, A. M., Meunier, N., Rubini, P., et al. 2019, *Nature Astronomy*, 3, 1135
 Lecavelier des Etangs, A., Cros, L., Hébrard, G., et al. 2022, *Scientific Reports*, 12, 5855
 Manfroid, J., Hutsemékers, D., & Jehin, E. 2021, *Nature*, 593, 372
 Meléndez, M., Bautista, M. A., & Badnell, N. R. 2007, *A&A*, 469, 1203
 Miret-Roig, N., Galli, P. A. B., Brandner, W., et al. 2020, *A&A*, 642, A179
 Montgomery, S. L. & Welsh, B. Y. 2012, *PASP*, 124, 1042
 Nilsson, H., Ljung, G., Lundberg, H., & Nielsen, K. E. 2006, *A&A*, 445, 1165
 Nowak, M., Lacour, S., Lagrange, A. M., et al. 2020, *A&A*, 642, L2
 Rebollido, I., Eiroa, C., Montesinos, B., et al. 2020, *A&A*, 639, A11
 Rebollido, I., Stark, C. C., Kammerer, J., et al. 2024, *AJ*, 167, 69
 Roberge, A., Feldman, P. D., Weinberger, A. J., Deleuil, M., & Bouret, J.-C. 2006, *Nature*, 441, 724
 Smith, B. A. & Terrile, R. J. 1984, *Science*, 226, 1421
 Strøm, P. A., Bodewits, D., Knight, M. M., et al. 2020, *PASP*, 132, 101001
 Tobin, W., Barnes, S. I., Persson, S., & Pollard, K. R. 2019, *MNRAS*, 489, 574
 Vidal-Madjar, A., Hobbs, L. M., Ferlet, R., Gry, C., & Albert, C. E. 1986, *A&A*, 167, 325
 Vidal-Madjar, A., Lagrange-Henri, A. M., Feldman, P. D., et al. 1994, *A&A*, 290, 245
 Vrignaud, T. & Lecavelier des Etangs. 2024, *A&A*
 Vrignaud, T., Lecavelier des Etangs, A., Kiefer, F., et al. 2024a, *A&A*, 684, A210
 Vrignaud, T., Lecavelier des Etangs, A., Strom, P. A., et al. 2024b, *The C/Fe and dust-to-ice ratios in Beta Pictoris exocomets*, HST Proposal. Cycle 32, ID. #17790
 Zieba, S., Zwintz, K., Kenworthy, M. A., & Kennedy, G. M. 2019, *A&A*, 625, L13

Appendix A: Ionisation state

Let X be a given chemical element (Fe, Al, Ca...). Assuming that X and Al are present in solar abundances in exocometary tails, and that most of the Aluminium gas is either singly or doubly ionised, we have:

$$\frac{s_X}{s_{Al}} = \left[\frac{X}{Al} \right]_{\odot} = \frac{[X]_e}{[Al II]_e + [Al III]_e} = \frac{\left[\frac{X}{X II} \right]_e}{\left[\frac{Al II}{X II} \right]_e + \left[\frac{Al III}{X II} \right]_e},$$

or equivalently:

$$\left[\frac{X II}{X} \right]_e = \frac{s_{Al}}{s_X} \cdot \left(\left[\frac{Al II}{X II} \right]_e + \left[\frac{Al III}{X II} \right]_e \right)^{-1},$$

where $s_{Al} = [Al/Fe]_{\odot}$ and $s_X = [X/Fe]_{\odot}$, and where the index e refers to exocometary abundances. Assuming that $[X II/Fe II]_e = \eta_X s_X$ and $[Al II/Fe II]_e = \eta_{Al} s_{Al}$, with η_X and η_{Al} fixed values common to all exocomets (as found for singly ionised species, Fig. 5), we have:

$$\left[\frac{Al II}{X II} \right]_e = \frac{\eta_{Al} s_{Al}}{\eta_X s_X}, \quad \left[\frac{Al III}{X II} \right]_e = \frac{1}{\eta_X s_X} \left[\frac{Al III}{Fe II} \right]_e,$$

yielding:

$$\left[\frac{X II}{X} \right]_e = \left(\frac{\eta_{Al}}{\eta_X} + \frac{1}{\eta_X s_{Al}} \left[\frac{Al III}{Fe II} \right]_e \right)^{-1}. \quad (A.1)$$

Provided that η_X can be estimated from measurements in many exocomets, Eq. A.1 allows us to convert the measured $Al III/Fe II$ ratio of a given exocomet into its $X II/X$ ratio. As an example, Fig. A.1 provides the $Ca II/Ca$, $Fe II/Fe$ and $Al II/Al$ ratios of our cometary exocomet sample (when the $Al III/Fe II$ ratio could be measured), using η values of 0.081 for Ca, 1 for Fe and 1.5 for Al (Table 2).

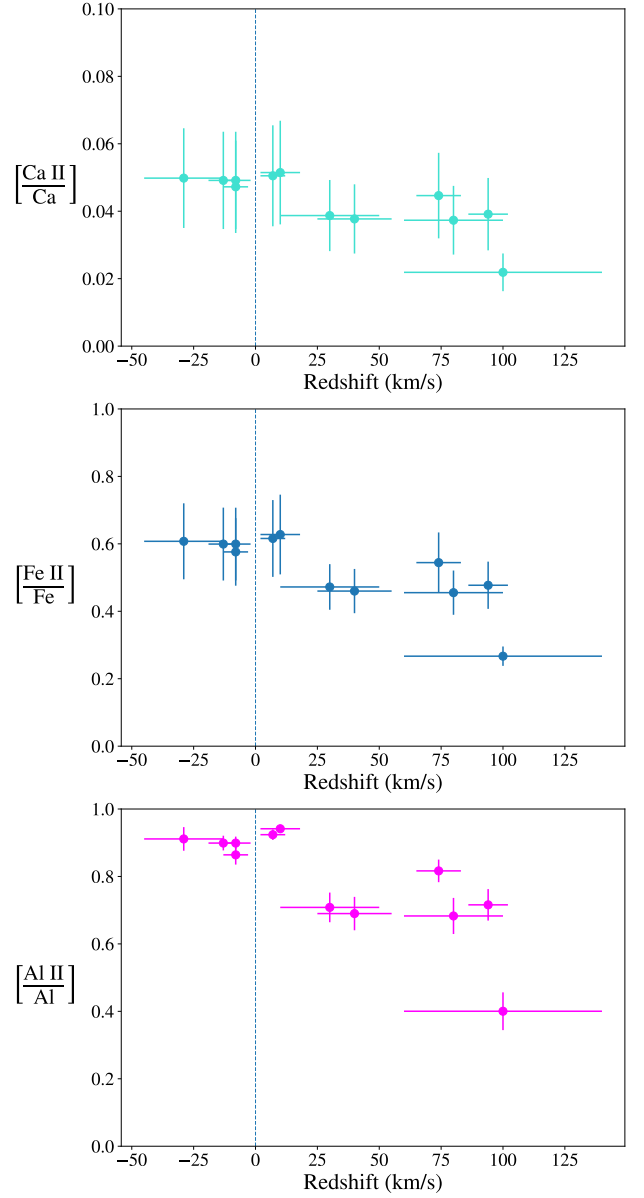


Fig. A.1: Estimates of the $Ca II/Ca$ (top), $Fe II/Fe$ (middle) and $Al II/Al$ (bottom) ratios of the studied exocomets, using Eq. A.1 and the measured $Al III/Fe II$ ratios. Error bars reflect uncertainties on the measured $Al III/Fe II$ ratios, and on the fixed parameters of Eq. A.1 (see Table 2).

Appendix B: Observations

Table B.1: Log of the 11 observations of β Pic from which our cometary sample was extracted. Other observations, not listed below, were used to reconstruct the EFS.

Date	Instrument	Program ID	Wavelength (Å)	Start time (UT)	Exposure time (s)	RV ranges showing comet absorption (km/s) ^a
1997-12-06	STIS	7512	1463 - 1661	07:18	900	[-4;+200]
			1628 - 1902	07:48	679	
			1879 - 2150	07:42	80	
			2128 - 2396	09:16	288	
			2377 - 2650	09:02	360	
			2620 - 2888	08:48	360	
	MJUS		3900 - 4000	09:24	1800	
1997-12-19	STIS	7512	1463 - 1661	19:51	900	[-17;+19], [+50;+150]
			1628 - 1902	20:22	679	
			1879 - 2150	20:14	80	
			2128 - 2396	21:53	288	
			2377 - 2650	21:40	360	
			2620 - 2888	21:26	360	
2001-08-27	STIS	9154	1628 - 1897	01:15	210	[-17;-3]
2002-05-22	STIS	9154	2327 - 2606	17:09	200	[-8,40]
2017-10-09	STIS	14735	2665 - 2931	23:40	475	[-35;+120]
2018-03-07	STIS	14735	2665 - 2931	02:33	475	[-40;+13]
2018-10-29	COS	15479	1163 - 1480	23:15	2012	[-30;-4], [+8;+140]
	STIS	15479	2665 - 2931	21:49	2101	
2018-12-15	COS	15479	1163 - 1480	05:50	2101	[-40;+50]
	STIS	15479	2665 - 2931	04:22	2101	
	HARPS	0102.C-0584	3783 - 6913	05:38	540	
2024-04-17	STIS	17421	1629 - 1897	00:09	1886	[-17;+100]
			1629 - 1897	01:36	2392	
			1629 - 1897	03:11	2392	
	HARPS	112.26ZF	3783 - 6913	23:12 ^b	10800	
2024-07-31	STIS	17421	1629 - 1897	11:42	1886	[-65;-5], [+3;+100]
			1629 - 1897	13:09	2392	
			1629 - 1897	14:44	2392	
2024-08-08	STIS	17421	1629 - 1897	11:03	1886	[-55,-15], [+2,+35], [+62,+140]
			1629 - 1897	12:17	1886	
			1629 - 1897	13:51	2392	
			1629 - 1897	15:26	2392	
	HARPS	112.26ZF	3783 - 6913	09:51	2400	

^a The RV ranges apply to all exposures of each visit.^b On April 16, 2024

Appendix C: Line examples

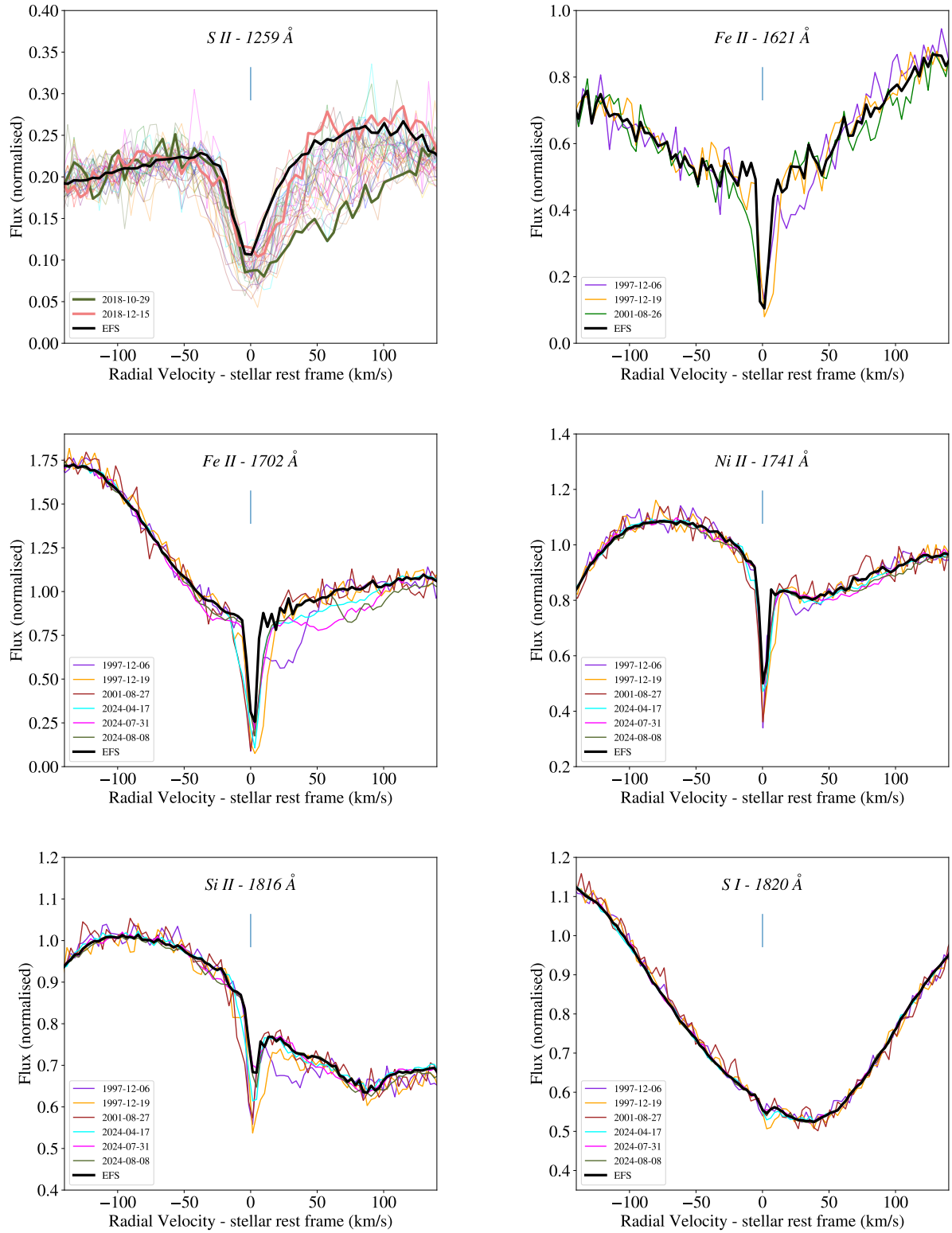


Fig. C.1: Examples of spectral lines used in our study. For conciseness, we show only one line for each series provided in Tab. G.1.

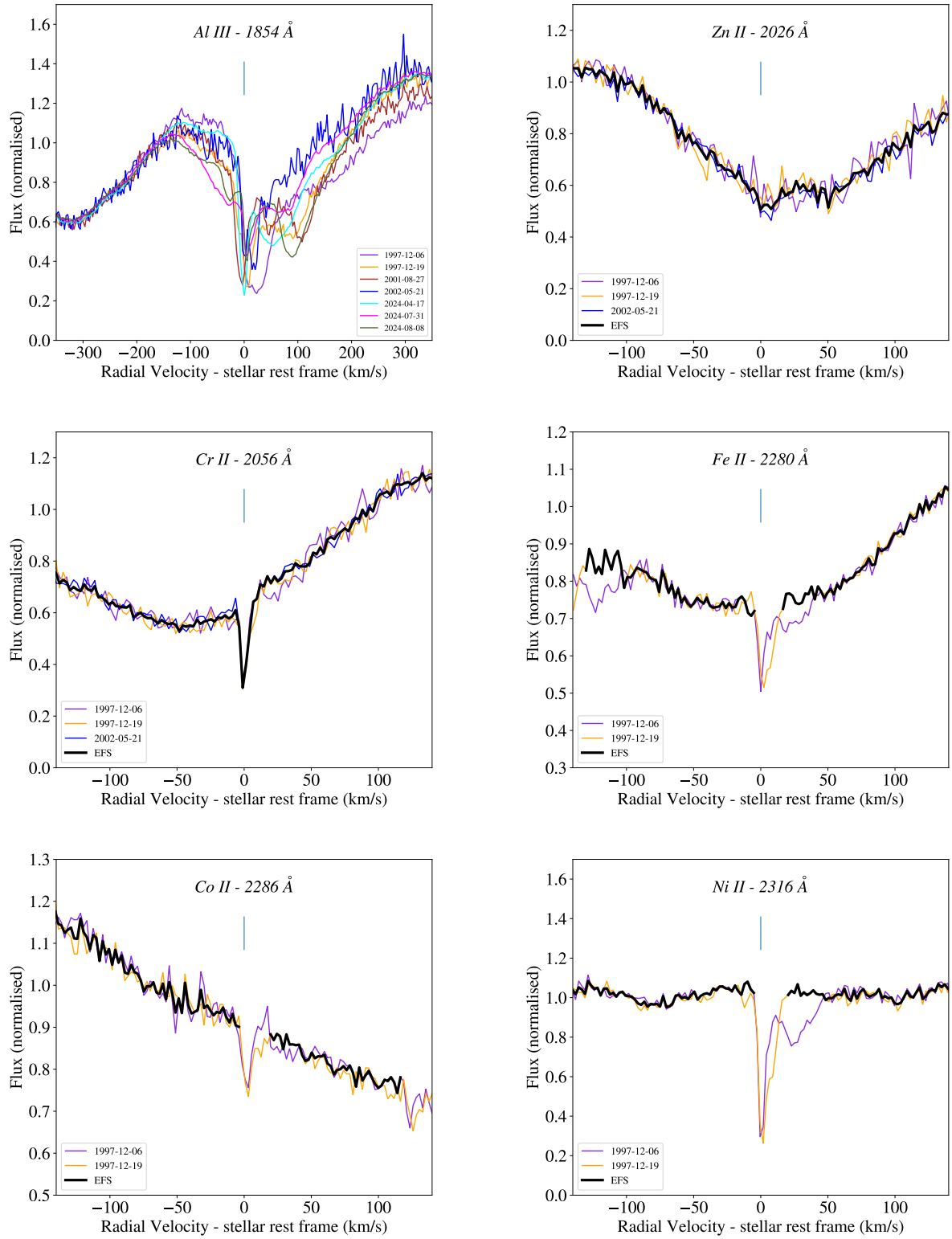


Figure C.1, continued.

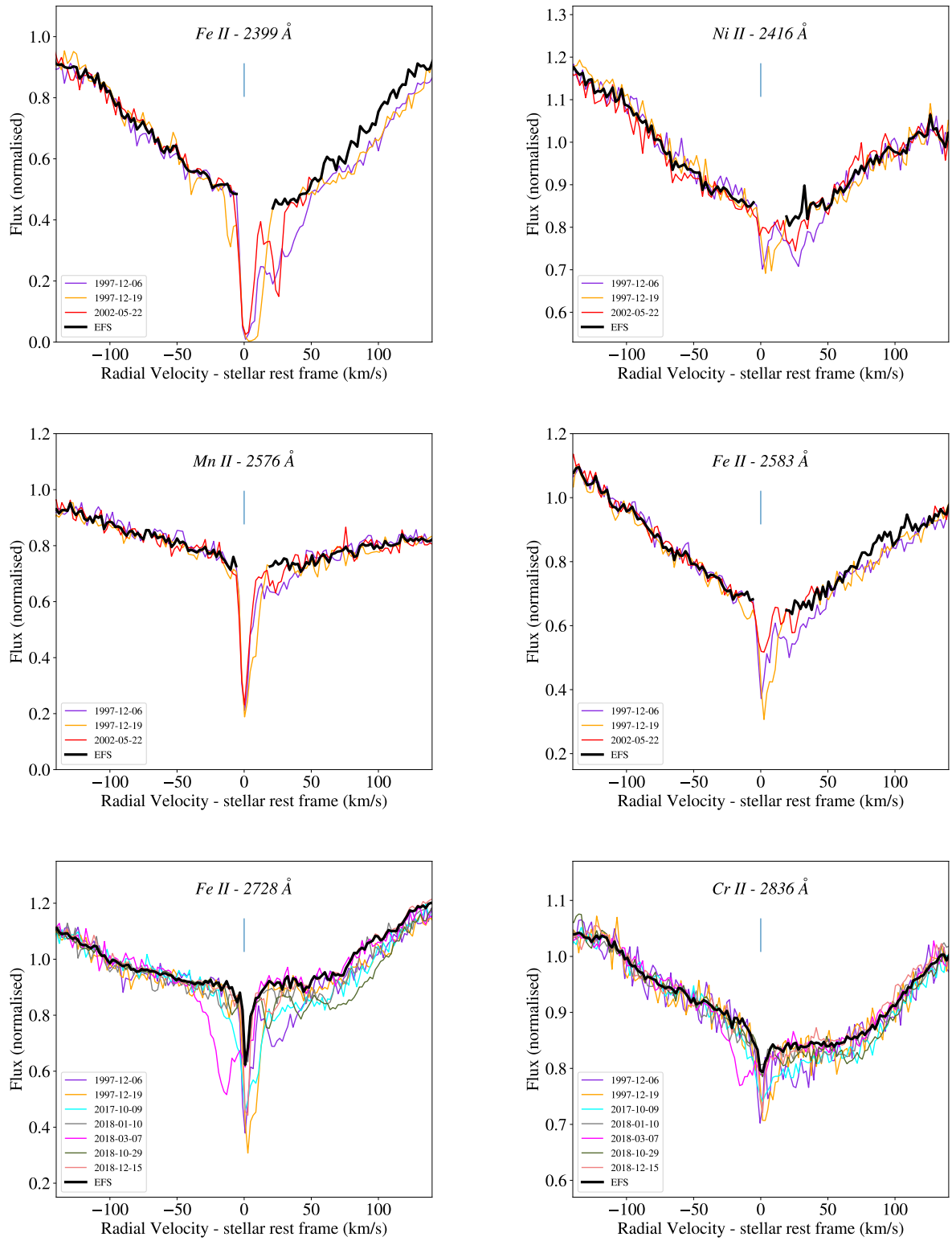


Figure C.1, continued.

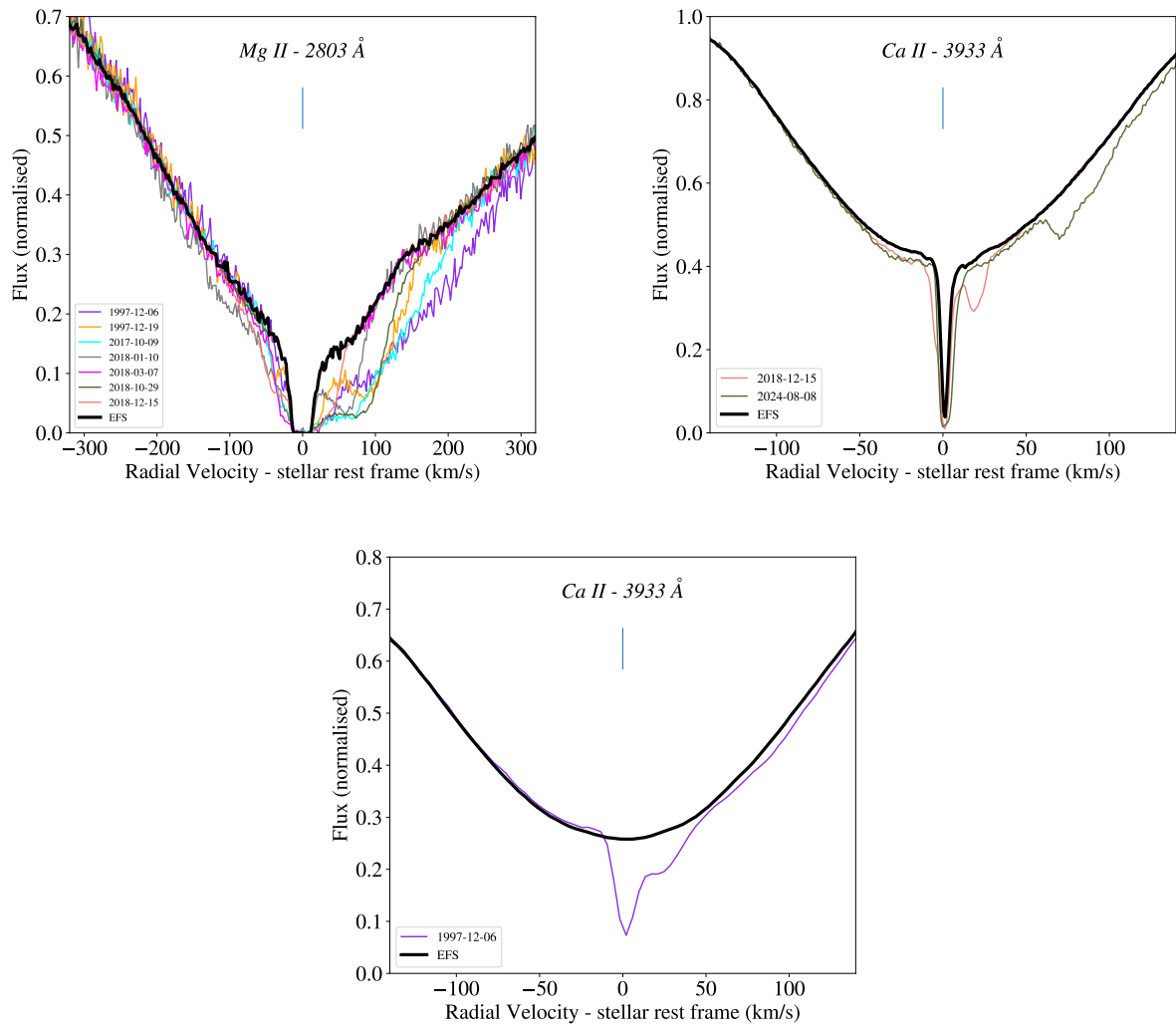


Figure C.1, continued Note that the $Ca II$ doublet (3900 \AA) was observed both by with HARPS (upper right) and MJUO (lower).

Appendix D: Comet list

Table D.1: List of the 29 comets studied in the present paper.

Label	Date (orbit ^a)	Nomenclature ^b	Total RV range ^c (km/s)	Fitted RV range ^d (km/s)	Studied lines ^e
1 ^f	1997-12-06	C19971206 a	[+10,+50]	[+21,+42]	Fe II λ 2250, λ 2400, λ 2600, λ 2750 Å Ni II λ 1750, λ 2200, λ 2400 Å Cr II λ 2000, λ 2700 Å Si II λ 1800 Å Co II λ 2300 Å Mn II λ 2600 Å S I λ 1800 Å Al III λ 1850 Å Zn II λ 2000 Å Ca II λ 3900 Å
2	1997-12-06	C19971206 b	[+60,+200]	[+70,+150]	Fe II λ 2400, λ 2600, λ 2750 Å Mg II λ 2800 Å Ca II λ 3900 Å
3	1997-12-19	C19971219 a	[-45,-31]	[-43,-33]	Fe II λ 2400, λ 2600, λ 2750 Å Ni II λ 1700, λ 2200, Ni II λ 2400 Å
4	1997-12-19	C19971219 b	[-17,-6]	[-16,-7]	Fe II λ 2250, λ 2400, λ 2600, λ 2750 Å Ni II λ 1700, λ 2200, λ 2400 Å Mn II λ 2600 Å Al III λ 1850 Å
5 ^g	1997-12-19	C19971219 c	[0,+19]	[+3,+15]	Fe II λ 1600, λ 1700, λ 2750 Å Mn II λ 2600 Å Ni II λ 1700 Å Cr II λ 2700 Å Si II λ 1800 Å S I λ 1800 Å Al III λ 1850 Å
6	1997-12-19	C19971219 d	[+50,+150]	[+60,+120]	Fe II λ 2400, λ 2600, λ 2750 Å Al III λ 1850 Å Mg II λ 2800 Å

^a Specific HST orbits used to analyse comets 20-29 (see Sect. 4.3).^b The full nomenclature should also contain the stellar name, e.g. " β Pic C19971206 a" for comet 1, as proposed by Lecavelier des Etangs et al. (in prep).^c RV range where each comet is detected.^d RV range used to measure the comets absorption depths.^e Fitted line series for each comet.^f Comet 1 was already studied in Vrignaud et al. (2024a).^g For comet 5, the Mn II/Fe II ratio was estimated from the λ 2600 Å Mn II and λ 2400-2600 Å Fe II line series, using the 2002-05-22 spectrum as a reference.

Table D.1, continued.

Label	Date (orbit)	Nomenclature	Total RV range (km/s)	Fitted RV range (km/s)	Studied lines
7	2001-08-27	C20010827 a	[-15,0]	[-13,-6]	Fe II λ 1700, λ 2600, λ 2750 Å Al III λ 1850 Å Mg II λ 2800 Å
8	2002-05-22	C20020522 a	[+18,+31]	[+21,+29]	Fe II λ 2400, λ 2600 Å Ni II λ 2400 Å Mn II λ 2600 Å
9	2017-10-09	C20171009 a	[+2,+15]	[+4,+12]	Fe II λ 2750 Å Cr II λ 2700 Å
10	2017-03-07	C20170307 a	[-20,-6]	[-35,0]	Fe II λ 2750 Å Cr II λ 2700 Å
11	2018-10-29	C20181029 a	[-22,-5]	[-22,-5]	Fe II λ 2750 Å S II λ 1250 Å Cr II λ 2700 Å
12	2018-10-29	C20181029 b	[+11,+28]	[+11,+28]	Fe II λ 2750 Å S II λ 1250 Å Cr II λ 2700 Å
13	2018-10-29	C20181029 c	[+30,+50]	[+30,+50]	Fe II λ 2750 Å S II λ 1250 Å Cr II λ 2700 Å
14 ^h	2018-10-29	C20181029 d	[+50,+150]	[+60,+90]	Fe II λ 2750 Å S II λ 1250 Å Cr II λ 2700 Å
15	2018-12-15	C20181215 a	[-50,-20]	[-50,-30]	Fe II λ 2750 Å Mg II λ 2800 Å Ca II λ 3900 Å
16	2018-12-15	C20181215 b	[-11,-3]	[-12,-6]	Fe II λ 2750 Å Ca II λ 3900 Å
17 ⁱ	2018-12-15	C20181215 c	[-2,+5]	[-2,+5]	Fe II λ 2750 Å Cr II λ 2700 Å
18	2018-12-15	C20181215 d	[+12,+32]	[+13,+28]	Fe II λ 2750 Å S II λ 1250 Å Cr II λ 2700 Å Ca II λ 3900 Å
19	2018-12-15	C20181215 e	[+32,+55]	[+32,+46]	Fe II λ 2750 Å Mg II λ 2800 Å Ca II λ 3900 Å

^h Comet 14 was also studied in Vrignaud et al. (2024a).ⁱ For comets 17 and 22, the much poorer EFS determination of Fe II lines compared to Ca II makes the retrieval of the Ca II/Fe II ratio hazardous.

Table D.1, continued.

Label	Date (orbit)	Nomenclature	Total RV range (km/s)	Fitted RV range (km/s)	Studied lines
20	2024-04-17 (1-3)	C20240417 a	[-14,-5]	[-12,-6]	Fe II λ 1700Å Ni II λ 1700Å Si II λ 1800Å S I λ 1800Å Al III λ 1850Å Ca II λ 3900Å
21 ^f	2024-04-17 (1-3)	C20240417 b	[+2,+11]	[+2,+11]	Fe II λ 1700Å Ni II λ 1700Å Si II λ 1800Å S I λ 1800Å Al III λ 1850Å
22	2024-04-17 (2)	C20240417 c	[+24,+58]	[+25,+55]	Fe II λ 1700Å Ni II λ 1700Å Si II λ 1800Å Al III λ 1850Å Ca II λ 3900Å
23	2024-04-17 (1)	C20240417 d	[+60,+104]	[+60,+95]	Fe II λ 1700Å Al III λ 1850Å Ca II λ 3900Å
24 ^j	2024-07-31 (1-3)	C20240731 a	[-60,-10]	[-40,-15]	Fe II λ 1700Å Ni II λ 1700Å Si II λ 1800Å
25 ^j	2024-07-31 (2)	C20240731 b	[+40,+75]	[+45,+70]	Fe II λ 1700Å Ni II λ 1700Å Si II λ 1800Å
26 ^j	2024-07-31 (3)	C20240731 c	[+70,+105]	[+78,+102]	Fe II λ 1700Å Ni II λ 1700Å
27	2024-08-08 (1-3)	C20240808 a	[-50,-10]	[-40,-15]	Fe II λ 1700Å Ni II λ 1700Å Si II λ 1800Å Al III λ 1850Å Ca II λ 3900Å
28	2024-08-08 (1-3)	C20240808 b	[+60,+85]	[+67,+83]	Fe II λ 1700Å Ni II λ 1700Å Si II λ 1800Å Al III λ 1850Å Ca II λ 3900Å
29	2024-08-08 (1-3)	C20240808 c	[+85,+105]	[+85,+100]	Fe II λ 1700Å Ni II λ 1700Å Si II λ 1800Å Al III λ 1850Å Ca II λ 3900Å

^j For comets 24 to 26, the Al III doublet was removed from the analysis, due to many overlapping absorption features.

Appendix E: Comet plots and curves of growth

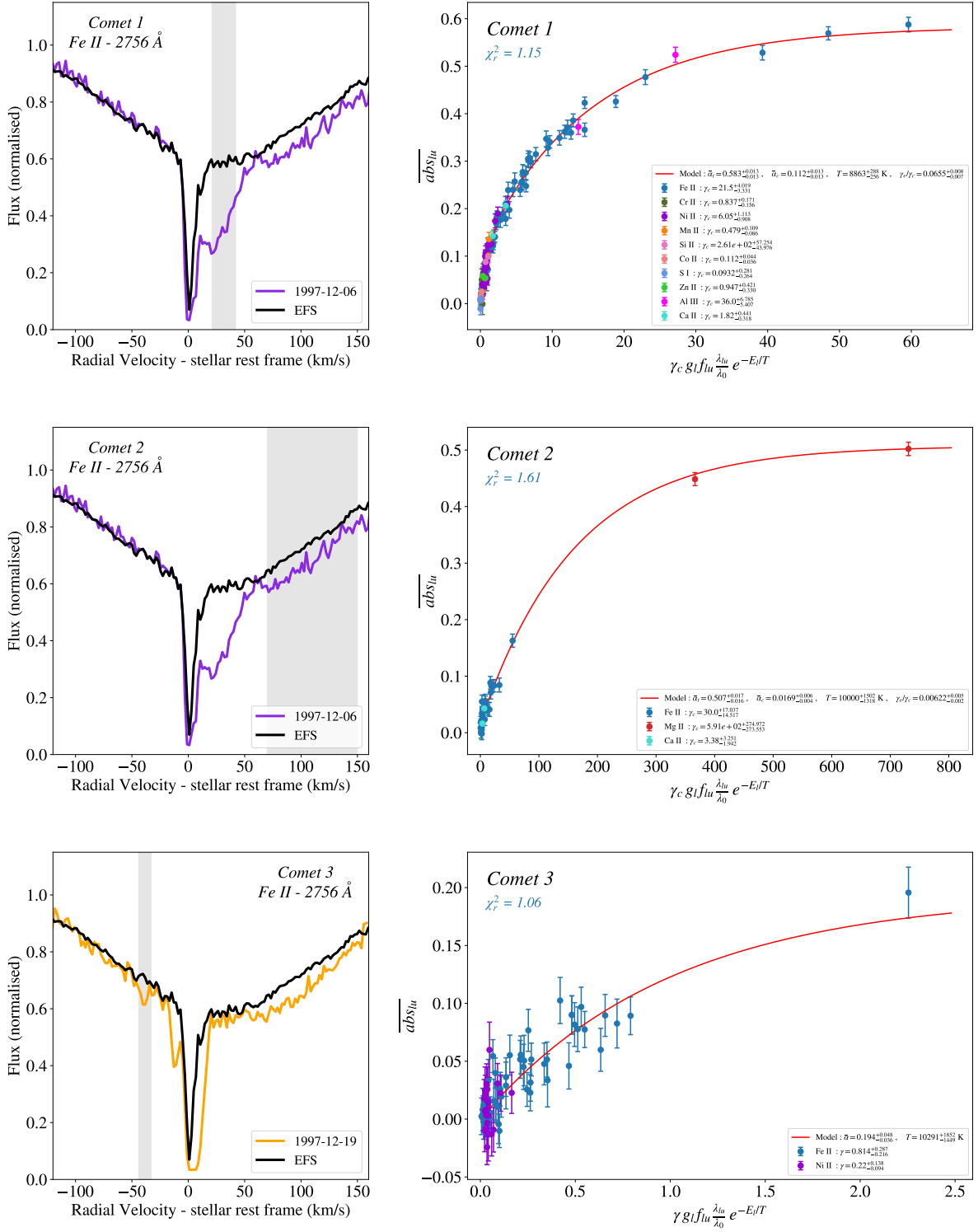


Fig. E.1: **Left** : plots of the 29 studied comets, in one strong Fe II line. The grey areas indicate the radial velocity range used to measure the absorption depth of each comet. For comets studied using a specific HST orbit (e.g. comets 23), the orbit number is indicated in parenthesis (e.g. '2024-04-17 (2)'). **Right** : curves of growth of the 29 studied comets. Different species are shown with different colours; the best-fit model is plotted with a red, solid line. The corresponding reduced χ^2 is also provided.

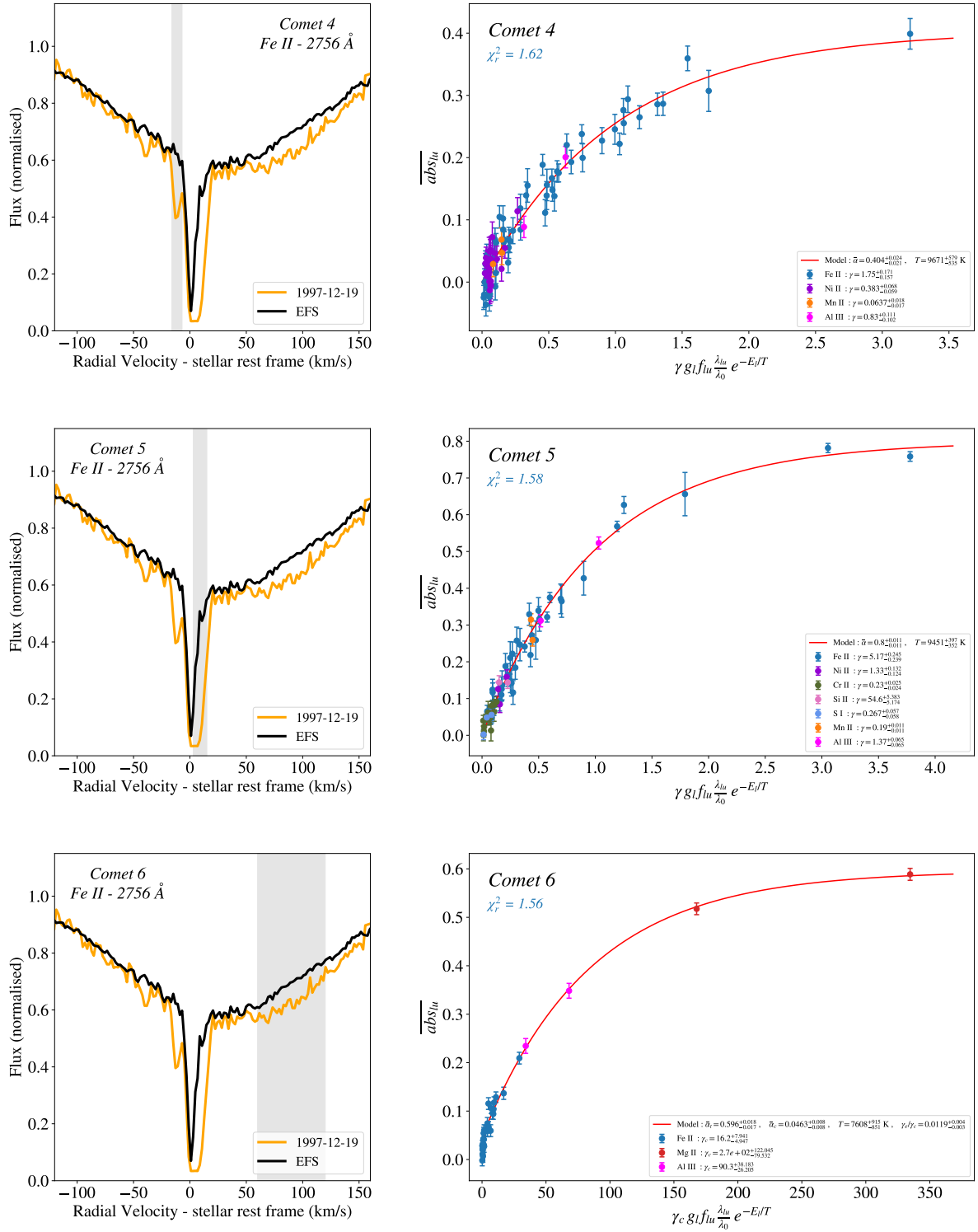


Figure E.1, continued.

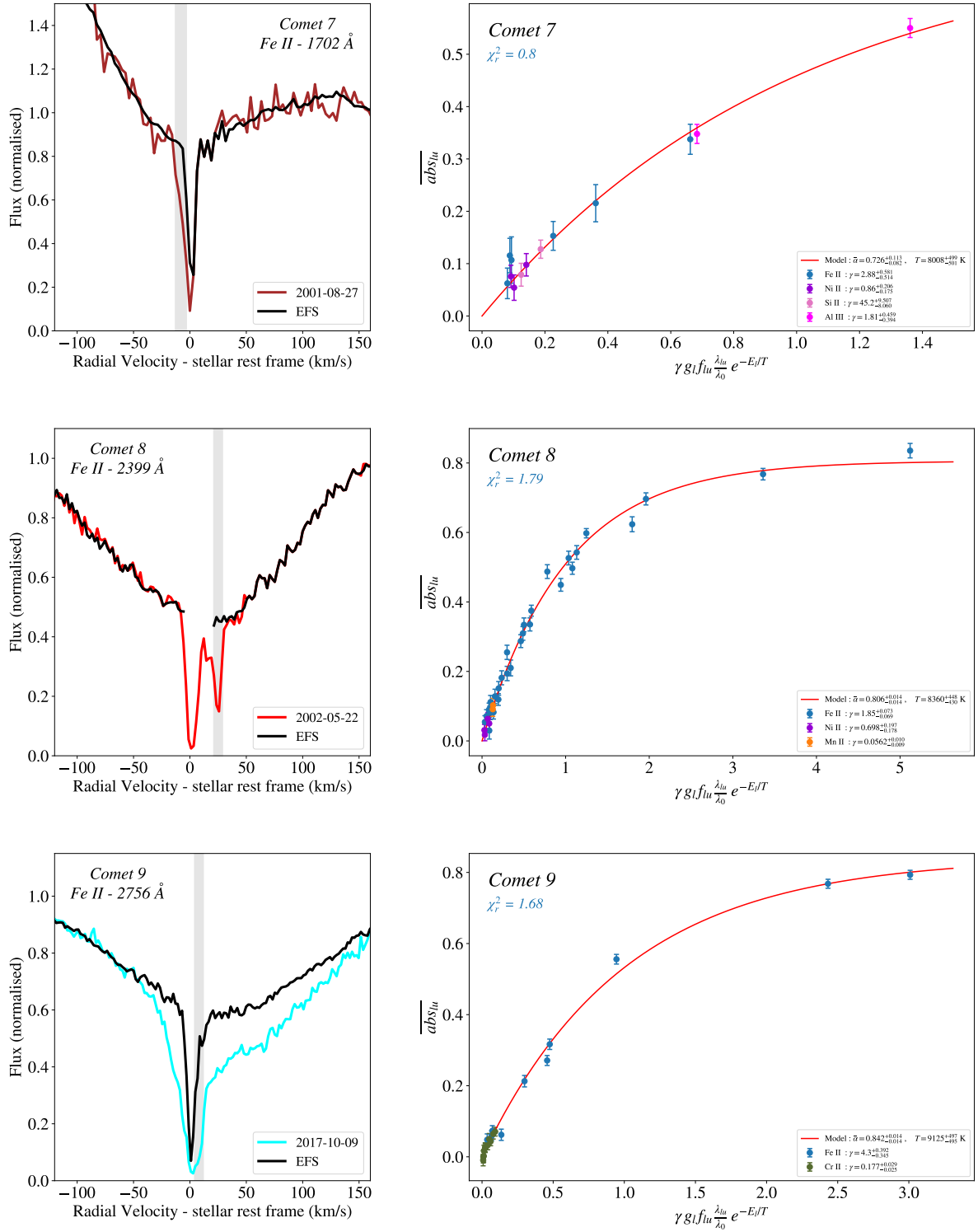


Figure E.1, continued.

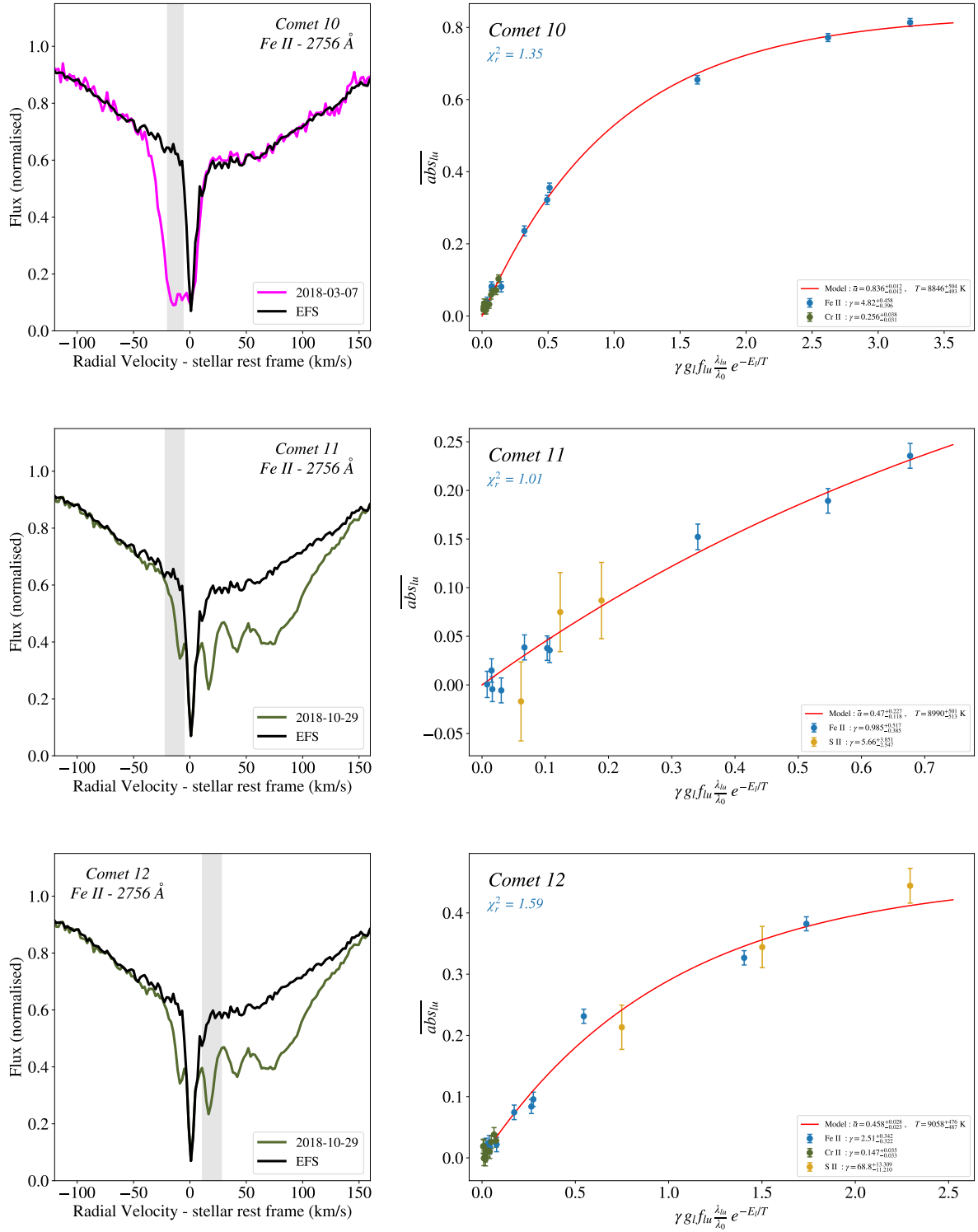


Figure E.1, continued.

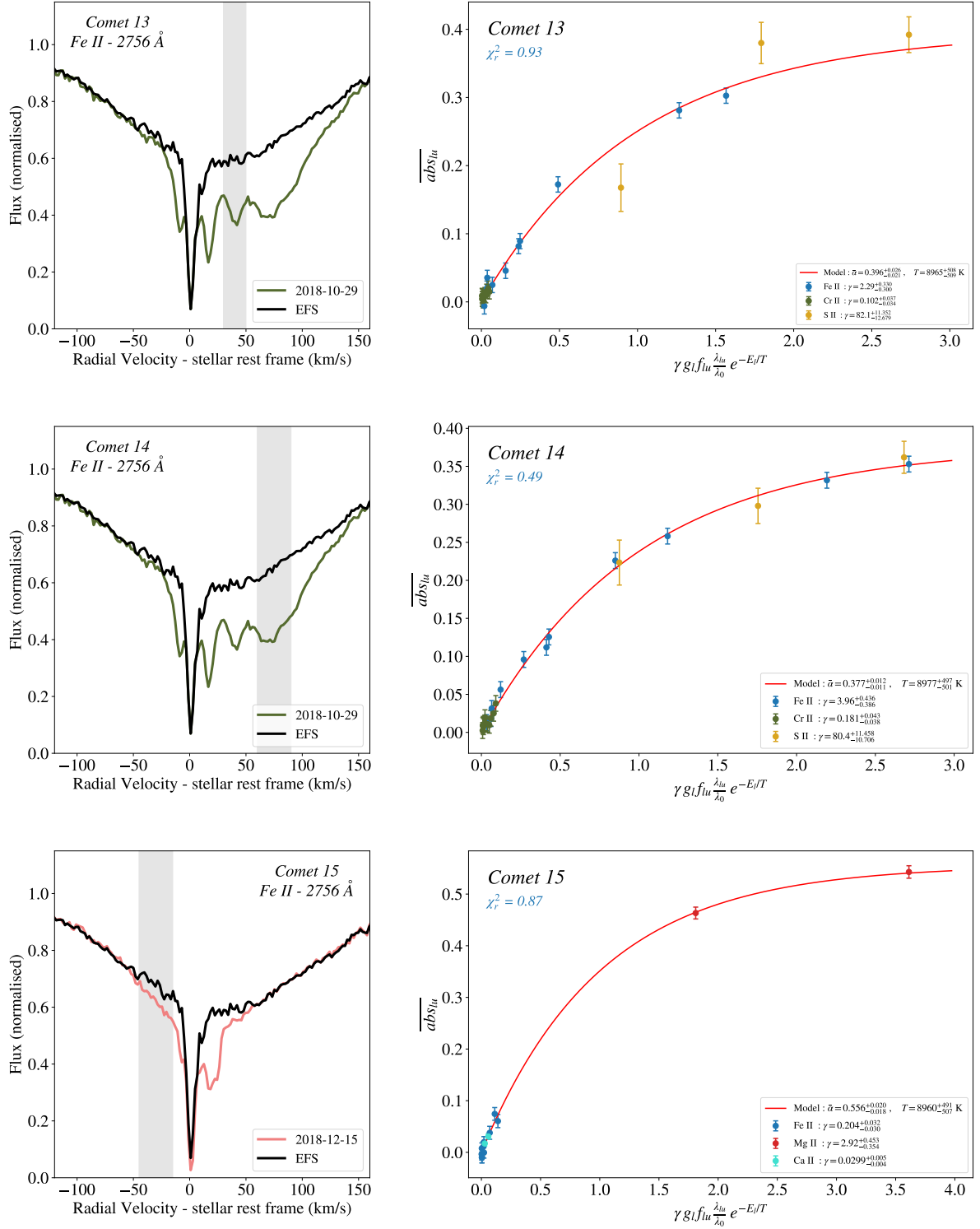


Figure E.1, continued.

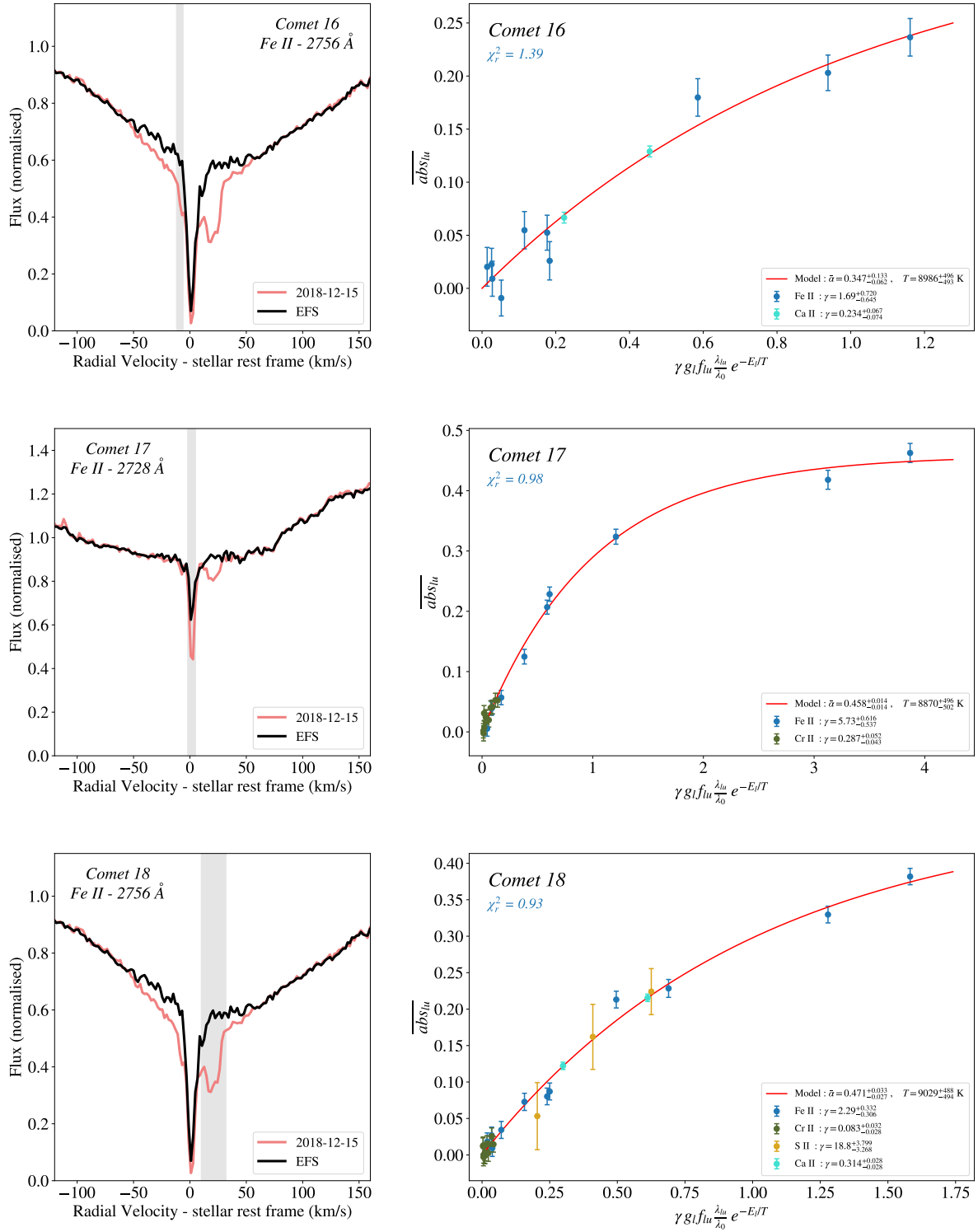


Figure E.1, continued.

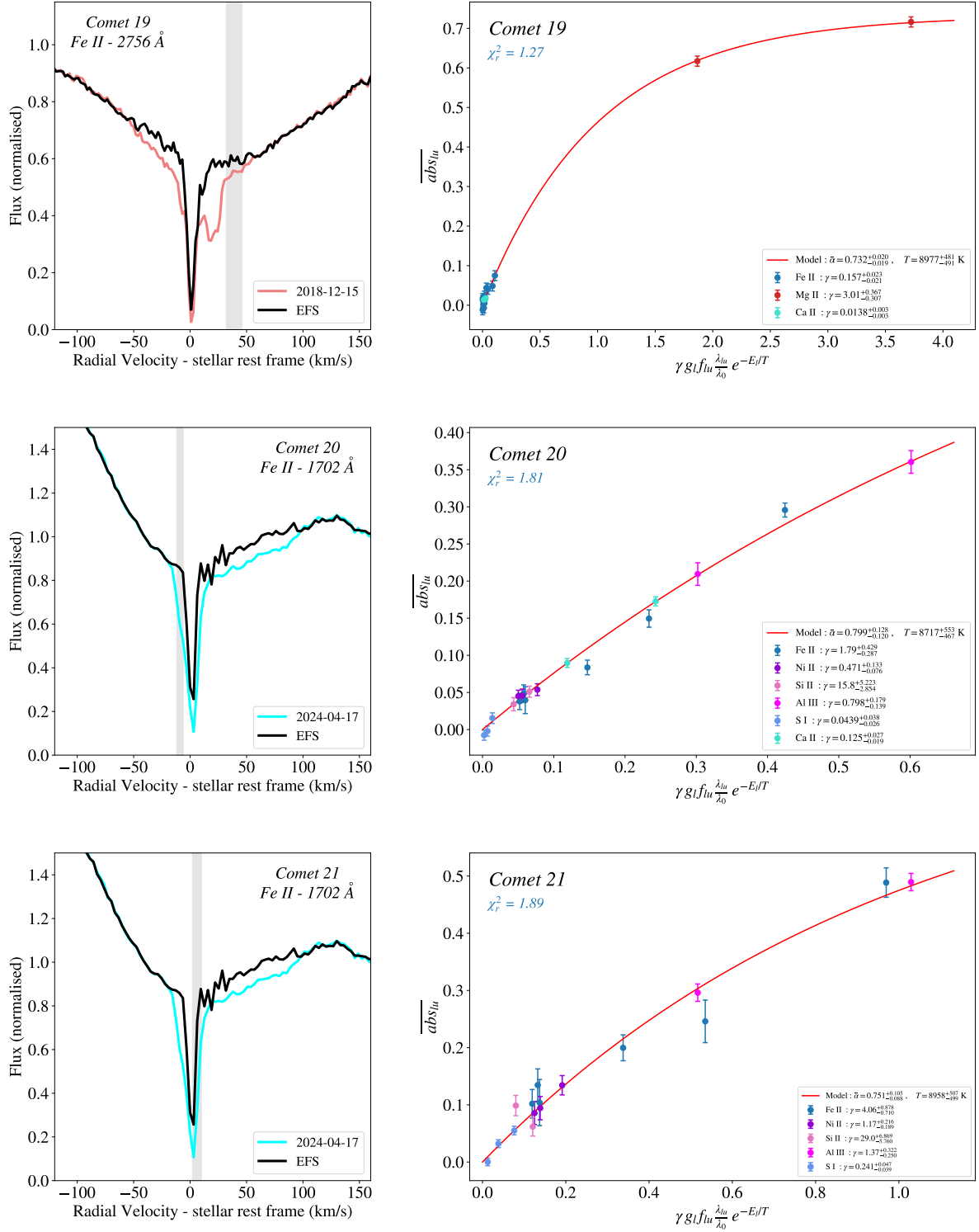


Figure E.1, continued.

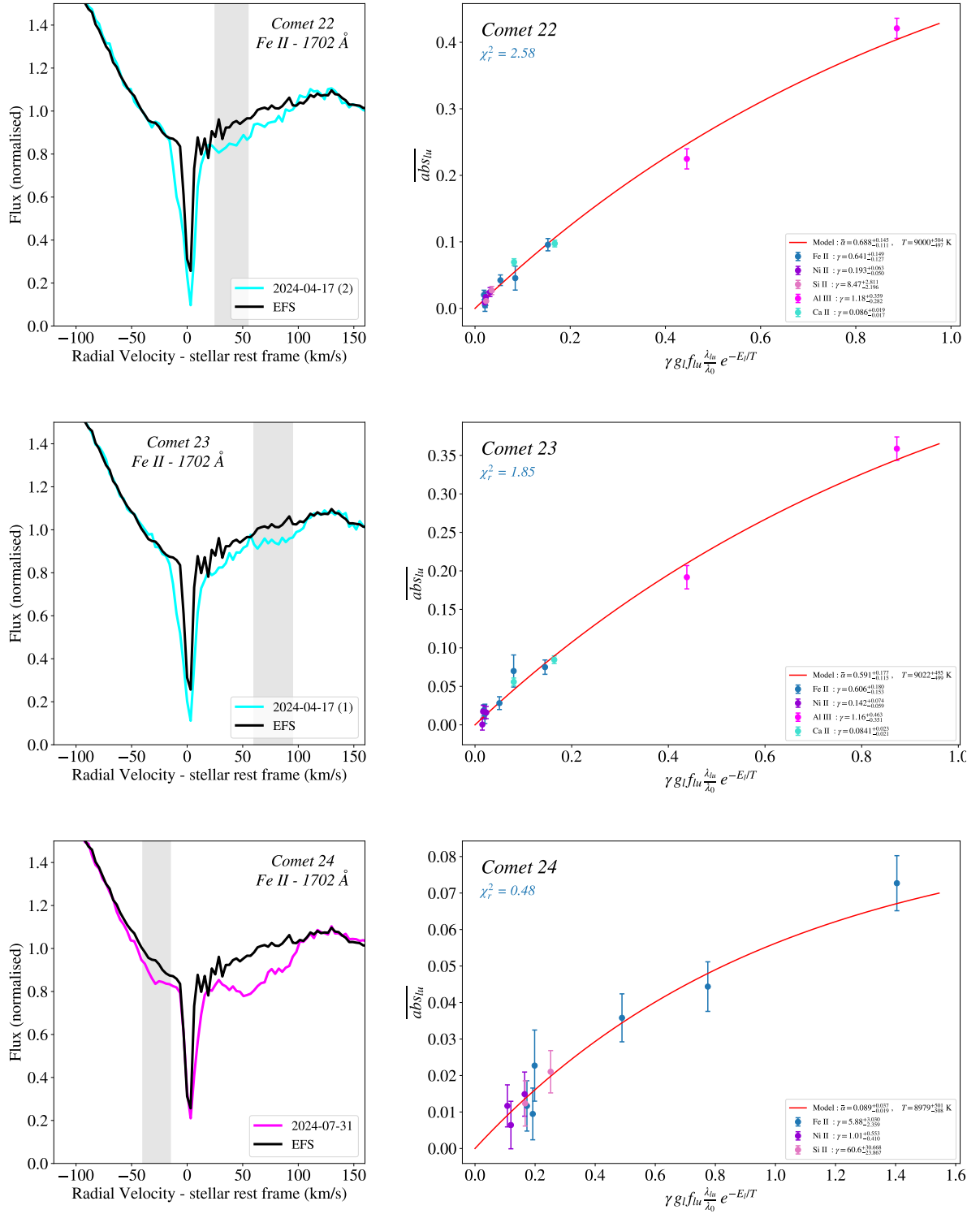


Figure E.1, continued.

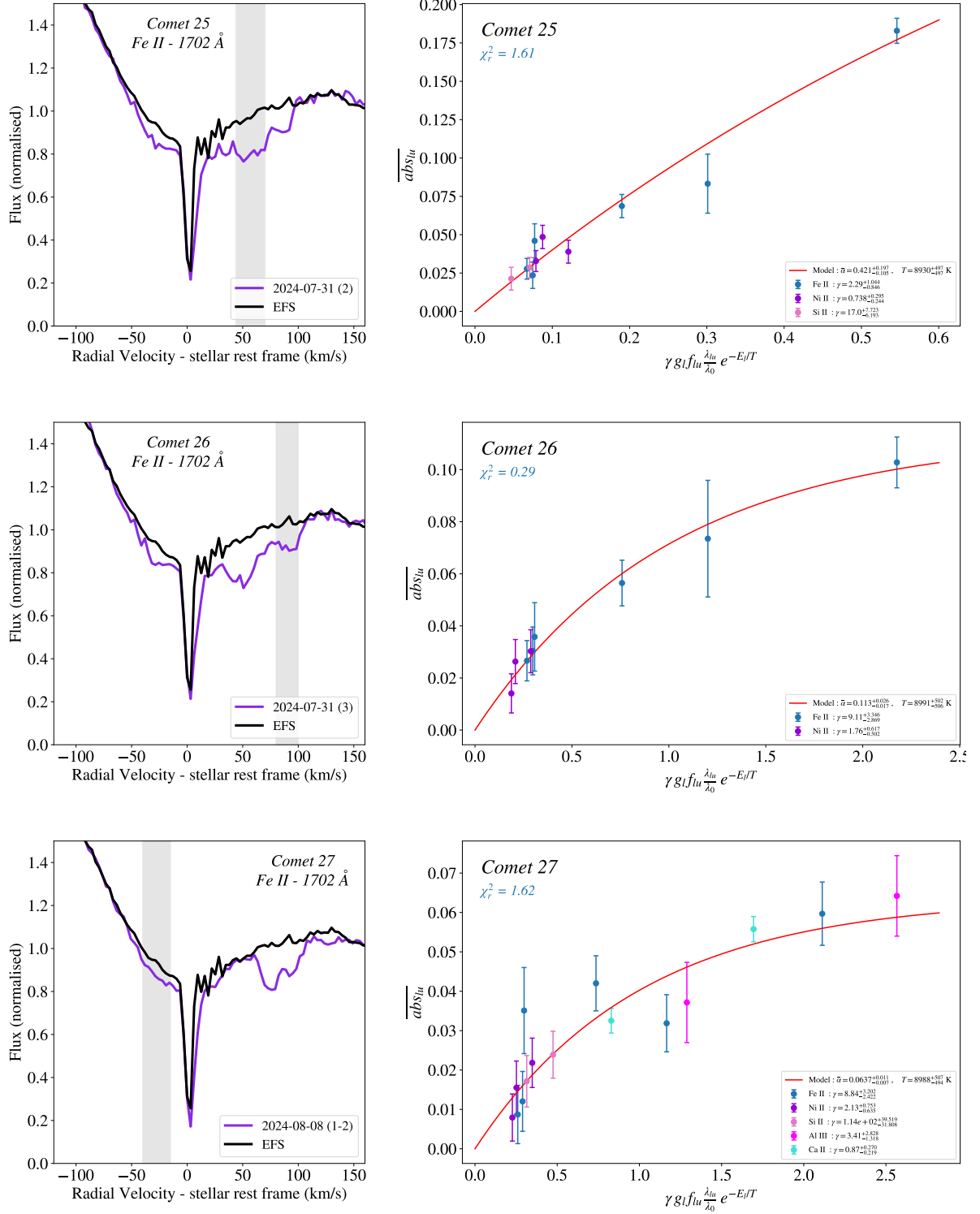


Figure E.1, continued.

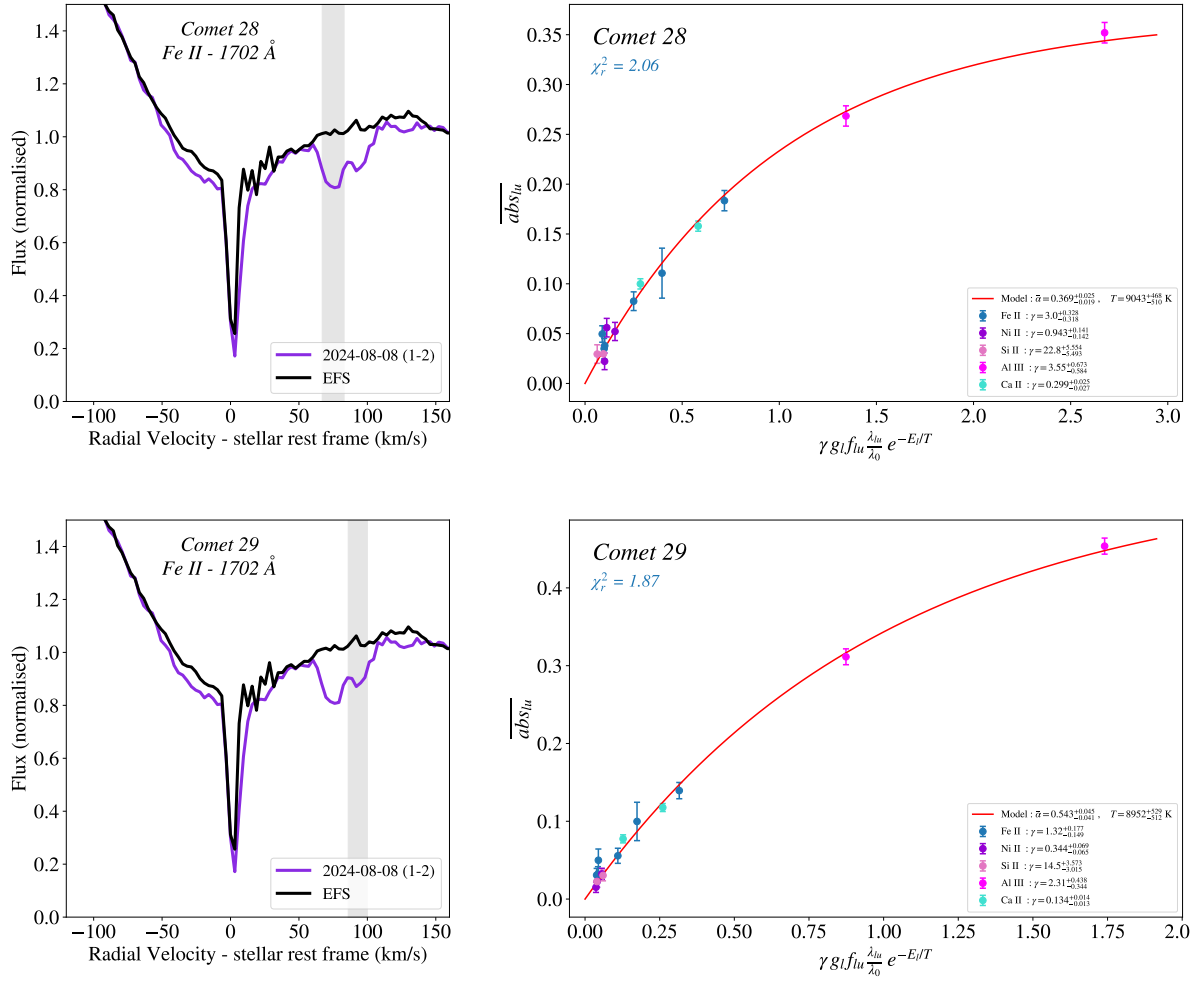


Figure E.1, continued.

Appendix F: Comet properties and composition

Table F.1: Fitted parameters of the cometary sample.

Label	$\bar{\alpha}^a$	$\log\left(\frac{N_{\text{tot, Fe II}}}{\Delta v}\right)$ ($\text{cm}^{-2} (\text{km s}^{-1})^{-1}$)	T_{ex}^b (K)
1	0.58 ± 0.01	13.40 ± 0.03	8900 ± 300
2	0.51 ± 0.02	$12.60^{+0.22}_{-0.14}$	10000 ± 1400
3	0.19 ± 0.04	12.18 ± 0.05	10300^{+1800}_{-1400}
4	0.40 ± 0.02	12.80 ± 0.02	9600 ± 600
5	0.80 ± 0.02	13.56 ± 0.02	9500 ± 400
6	0.60 ± 0.02	$12.81^{+0.13}_{-0.09}$	7600 ± 900
7	0.73 ± 0.10	13.23 ± 0.05	
8	0.81 ± 0.02	13.08 ± 0.02	8400 ± 400
9	0.84 ± 0.02	13.49 ± 0.02	
10	0.84 ± 0.02	13.52 ± 0.02	
11	$0.46^{+0.22}_{-0.11}$	12.60 ± 0.06	
12	0.46 ± 0.03	12.99 ± 0.03	
13	0.40 ± 0.04	12.89 ± 0.04	
14	0.38 ± 0.02	13.10 ± 0.03	
15	0.56 ± 0.02	11.98 ± 0.04	
16	$0.34^{+0.12}_{-0.06}$	12.70 ± 0.08	
17	0.46 ± 0.02	13.34 ± 0.03	
18	0.48 ± 0.03	12.96 ± 0.03	
19	0.73 ± 0.02	11.98 ± 0.06	
20	0.83 ± 0.11	13.08 ± 0.03	
21	$0.76^{+0.12}_{-0.09}$	13.41 ± 0.04	
22	$0.70^{+0.16}_{-0.12}$	12.60 ± 0.04	
23	$0.60^{+0.19}_{-0.12}$	12.48 ± 0.05	
24	$0.09^{+0.04}_{-0.02}$	12.63 ± 0.09	
25	$0.42^{+0.21}_{-0.11}$	12.91 ± 0.05	
26	$0.11^{+0.03}_{-0.02}$	12.94 ± 0.09	
27	0.06 ± 0.01	12.67 ± 0.10	
28	0.37 ± 0.02	12.98 ± 0.03	
29	0.55 ± 0.04	12.79 ± 0.04	

^a Replaced by $\bar{\alpha}_r$ for comets fitted with the two-component model (comets 1, 2 and 6).

^b As measured from the curve of growth fit. For comets where the excitation temperature could not be estimated (due to short wavelength coverage), a gaussian prior of 9000 ± 500 K was assumed.

Table F.2: Measured composition of each studied exocomet.

Comet	S^0/Fe^+ ($\cdot 10^{-3}$)	Ca^+/Fe^+ ($\cdot 10^{-3}$)	Mg^+/Fe^+	Mn^+/Fe^+ ($\cdot 10^{-3}$)	Si^+/Fe^+	Cr^+/Fe^+ ($\cdot 10^{-2}$)	Co^+/Fe^+ ($\cdot 10^{-3}$)	Zn^+/Fe^+ ($\cdot 10^{-3}$)	Ni^+/Fe^+ ($\cdot 10^{-2}$)	S^+/Fe^+	Al^{2+}/Fe^+ ($\cdot 10^{-2}$)
1	0.8 ± 2.0	0.45 ± 0.04		4.6 ± 0.7	1.19 ± 0.16	0.95 ± 0.15	4.1 ± 1.4	1.5 ± 0.5	8.1 ± 0.5		5.5 ± 0.4
2		0.64 ± 0.27	0.61 ± 0.14								
3									8.2 ± 3.2		
4				7.8 ± 2.1					6.4 ± 0.9		1.5 ± 0.2
5	8.1 ± 1.7			7.7 ± 0.7	0.97 ± 0.10	1.15 ± 0.10			6.6 ± 0.8		0.83 ± 0.04
6			0.60 ± 0.11								20 ± 2.6
7					1.55 ± 0.26				8.9 ± 1.7		2.1 ± 0.3
8				5.8 ± 1.0					10.6 ± 2.7		
9						1.02 ± 0.11					
10						1.27 ± 0.10					
11										0.50 ± 0.20	
12						1.43 ± 0.29				2.25 ± 0.32	
13						1.07 ± 0.33				3.08 ± 0.55	
14						1.11 ± 0.22				1.71 ± 0.27	
15		0.76 ± 0.14	0.48 ± 0.07								
16		0.72 ± 0.10									
17						1.20 ± 0.15					
18		0.72 ± 0.07				0.90 ± 0.30				0.68 ± 0.16	
19		0.46 ± 0.12	0.64 ± 0.10								
20	3.6 ± 2.2	0.36 ± 0.03			0.85 ± 0.12				7.4 ± 0.8		1.5 ± 0.1
21	9.5 ± 1.3				0.68 ± 0.13				8.1 ± 1.1		1.1 ± 0.1
22		0.70 ± 0.07			1.27 ± 0.30				8.7 ± 2.1		6.0 ± 0.7
23		0.73 ± 0.09							6.9 ± 2.8		6.2 ± 0.9
24					1.00 ± 0.32				5.2 ± 1.9		
25					0.71 ± 0.16				9.2 ± 1.3		
26									5.7 ± 1.6		
27		0.52 ± 0.10			1.23 ± 0.40				6.9 ± 2.3		1.3 ± 0.5
28		0.52 ± 0.04			0.72 ± 0.17				8.9 ± 1.3		3.0 ± 0.4
29		0.53 ± 0.05			1.02 ± 0.22				7.4 ± 1.4		5.0 ± 0.6

Appendix G: List of the studied lines

Table G.1: List of all spectral lines used in the study, grouped by series.

Series	λ_{lu}^a (Å)	E_l^a (cm ⁻¹)	E_l/k_B (K)	A_{ul}^a (10 ⁷ s ⁻¹)	$g_l f_{lu}$
S II $\lambda 1250\text{Å}$	1250.58	0	0	5.13	0.024
	1253.81	0	0	5.12	0.048
	1259.52	0	0	5.1	0.073
Fe II $\lambda 1600\text{Å}$	1608.45	0	0	19.1	0.59
	1612.81	1873	2694	6.60	0.31
	1618.47	385	554	5.53	0.174
	1621.68	385	554	13.2	0.31
	1625.52	2430	3497	4.00	0.158
	1629.16	668	961	7.20	0.172
	1631.13	668	961	6.93	0.111
	1633.91	2838	4083	3.90	0.125
	1634.35	863	1241	3.21	0.077
	1635.40	7955	11446	23.0	0.55
	1636.33	863	1241	9.63	0.155
	1637.40	1873	2694	3.60	0.116
	1639.40	977	1406	6.85	0.110
	1640.15	3117	4485	5.90	0.143
	1641.76	8392	12074	18.0	0.29
	1643.58	2430	3497	4.40	0.107
	1646.18	8680	12490	14.0	0.114
	1647.16	8392	12074	5.00	0.122
	1650.70	8847	12729	14.0	0.114
	1659.48	2430	3497	8.00	0.198
1663.22	1873	2694	6.70	0.111	
Fe II $\lambda 1700\text{Å}$	1696.80	1873	2694	1.70	0.073
	1702.05	1873	2694	10.0	0.52
	1708.62	2430	3497	2.00	0.070
	1713.00	2430	3497	7.10	0.31
	1720.61	2838	4083	5.90	0.21
	1726.39	3117	4485	3.20	0.086
Ni II $\lambda 1700\text{Å}^b$	1709.61	0	0	7.25	0.191
	1741.56	0	0	9.48	0.259
	1751.91	0	0	4.55	0.168
Si II $\lambda 1800\text{Å}^c$	1808.01	0	0	0.213	0.0042
	1816.93	287	413	0.222	0.0066
S I $\lambda 1800\text{Å}$	1807.31	0	0	32.7	0.48
	1820.34	396	570	17.1	0.26
	1826.25	573	824	5.64	0.085

^a Unless otherwise indicated, the level energies and line parameters (λ_{lu} , A_{ul} , f_{lu}) were collected from the NIST database (Kramida et al. (2023)). The uncertainties are typically of the order of 10 %.

^b Line parameters obtained from Boissé & Bergeron (2019).

^c Line parameters obtained from Bergeson & Lawler (1993).

Table G.1, continued.

Series	λ_{lu} (Å)	E_l (cm ⁻¹)	E_l/k_B (K)	A_{ul}^a (10 ⁷ s ⁻¹)	$g_l f_{lu}$
Al III λ 1850Å	1854.72	0	0	54.4	1.12
	1862.79	0	0	53.6	0.56
Zn II λ 2000Å	2026.14	0	0	40.7	1.00
	2062.66	0	0	38.6	0.49
Cr II λ 2000Å	2056.26	0	0	12.2	0.62
	2062.24	0	0	11.9	0.46
	2066.16	0	0	12.0	0.31
Ni II λ 2200Å	2166.23	8394	12077	24.0	1.69
	2169.77	9330	13424	15.8	0.89
	2175.35	9330	13424	14.3	1.01
	2175.82	10116	14555	17.7	0.75
	2185.29	10664	15343	29.0	0.83
	2202.09	10664	15343	13.0	0.57
	2207.41	10116	14555	16.6	0.97
	2211.07	9330	13424	3.9	0.29
	2217.17	8394	12077	34.0	3.01
	2223.64	8394	12077	9.8	0.73
	2225.56	9330	13424	16.5	0.98
	2227.02	10116	14555	13.0	0.58
	2254.55	10664	15343	19.8	0.91
	2265.16	10116	14555	14.3	0.88
	2270.91	9330	13424	15.6	1.21
	2279.47	13550	19496	28.0	1.31
	2287.79	14996	21576	28.0	0.88
	2297.26	13550	19496	19.8	1.25
2298.2	10664	15343	30.0	0.48	
2298.97	14996	21576	28.0	1.33	
2303.7	9330	13424	29.0	1.38	
2316.75	8394	12077	28.8	1.85	
Fe II λ 2250Å	2249.88	0	0	0.3	0.0182
	2251.63	668	961	0.319	0.0146
	2253.82	385	554	0.44	0.027
	2260.78	0	0	0.318	0.024
	2261.56	863	1241	0.216	0.0099
	2268.29	668	961	0.369	0.023
2280.62	385	554	0.449	0.035	
Co II λ 2300Å	2286.86	3350	4820	33.0	3.36
	2308.57	4028	5796	26.0	2.29
	2312.32	4560	6561	28.0	2.02
	2314.77	4950	7122	28.0	1.57
	2315.69	5205	7489	27.0	1.09

Table G.1, continued.

Series	λ_{lu} (Å)	E_l (cm ⁻¹)	E_l/k_B (K)	A_{ul}^a (10 ⁷ s ⁻¹)	$g_l f_{lu}$
	2328.11	667	960	6.6	0.22
	2332.02	1873	2694	3.17	0.21
	2333.51	385	554	13.1	0.64
	2338.73	863	1241	11.3	0.37
	2344.21	0	0	17.3	1.14
	2345.0	977	1406	9.27	0.31
	2348.83	1873	2694	6.5	0.43
	2349.02	668	961	11.5	0.57
	2355.61	2838	4083	2.67	0.089
	2359.83	863	1241	5.0	0.25
	2360.72	1873	2694	3.59	0.30
	2361.02	2430	3497	6.2	0.31
	2362.74	2430	3497	1.41	0.094
	2365.55	385	554	5.9	0.49
	2367.32	2838	4083	1.01	0.051
Fe II λ 2400Å	2369.32	2838	4083	6.06	0.20
	2371.22	3117	4485	1.73	0.058
	2374.46	0	0	4.25	0.36
	2375.92	3117	4485	9.8	0.166
	2380.00	2430	3497	2.73	0.185
	2381.49	668	961	3.1	0.21
	2382.76	0	0	31.3	3.20
	2385.11	3117	4485	3.2	0.109
	2389.36	385	554	10.5	0.72
	2392.21	2430	3497	0.377	0.032
	2396.35	385	554	25.9	2.23
	2399.97	668	961	13.9	0.72
	2405.62	668	961	19.6	1.36
	2407.39	863	1241	16.1	0.56
	2411.25	863	1241	15.5	0.81
	2411.80	977	1406	23.7	0.41
	2414.04	977	1406	10.2	0.36
	2395.25	13550	19496	17.0	1.46
Ni II λ 2400Å	2416.87	14996	21576	21.0	1.47
	2438.63	13550	19496	5.4	0.48
	2511.63	13550	19496	5.8	0.55
	2576.88	0	0	28.0	2.51
Mn II λ 2600Å	2594.50 ^d	0	0	27.6	1.95
	2606.46	0	0	26.9	1.37
	2563.30	7955	11446	17.9	1.06
	2564.24	8392	12074	15.1	0.60
	2567.68	8680	12490	11.0	0.22
Fe II λ 2600Å	2578.69	8847	12729	12.0	0.24
	2583.36	8680	12490	8.8	0.35
	2592.31	8392	12074	5.7	0.35
	2594.50 ^d	8847	12729	1.63	0.066

^d The optical depths of the 2594.50 Å Mn II and 2594.50 Å Fe II lines were added up together in the fits, the two lines being separated by 800 m/s only.

Table G.1, continued.

Series	λ_{lu} (Å)	E_l (cm ⁻¹)	E_l/k_B (K)	A_{ul}^a (10 ⁷ s ⁻¹)	gf_{lu}
	2586.65	0	0	8.94	0.72
	2599.15	385	554	14.3	0.87
	2600.17	0	0	23.5	2.38
	2607.87	668	961	17.3	0.71
	2612.65	385	554	12.0	0.98
Fe II $\lambda 2600\text{Å}$ (continued)	2614.6	863	1241	21.2	0.44
	2618.4	668	961	4.88	0.30
	2622.45	977	1406	5.6	0.115
	2626.45	385	554	3.52	0.36
	2629.08	977	1406	8.74	0.36
	2631.83	863	1241	8.16	0.51
	2632.11	668	961	6.29	0.52
	2669.50	12033	17313	14.5	0.31
	2672.60	12148	17478	10.9	0.47
	2673.62	12304	17703	5.74	0.37
	2677.95 ^e	12304	17703	11.9	1.02
	2677.95 ^e	12496	17980	20.9	2.25
	2679.59	12033	17313	8.02	0.52
Cr II $\lambda 2700\text{Å}$ ^f	2767.35	12496	17980	22.3	2.05
	2836.47	12496	17980	25.0	3.62
	2844.08	12304	17703	18.9	2.29
	2850.67	12148	17478	15.2	1.48
	2856.51	12033	17313	11.3	0.83
	2863.41	12304	17703	8.66	0.85
	2865.95	12148	17478	11.1	0.82
	2715.22	7955	11446	5.7	0.38
	2725.69	8392	12074	0.96	0.064
	2728.35	8392	12074	9.38	0.42
	2731.54	8680	12490	2.79	0.125
	2737.78	8680	12490	12.2	0.27
Fe II $\lambda 2750\text{Å}$	2740.36	7955	11446	22.1	1.99
	2744.01	8847	12729	19.7	0.89
	2747.3	8680	12490	20.5	1.39
	2747.79	8392	12074	16.9	1.15
	2756.55	7955	11446	21.5	2.45
	2762.66	8847	12729	1.38	0.063
	2769.75	8680	12490	0.48	0.033
Mg II $\lambda 2800\text{Å}$	2796.35	0	0	26.0	1.22
	2803.53	0	0	25.7	0.61
Ca II $\lambda 3900\text{Å}$	3934.77	0	0	14.7	1.36
	3969.59	0	0	14.0	0.66

^e The two Cr II lines at 2677.95 Å were considered as a single line, with an effective gf -value of 3.27.^f Line parameters obtained from Nilsson et al. (2006).